

# OPTICAL DIAGNOSTICS FOR PLASMA ARCS

JACOB A. PEARCY

A SENIOR THESIS

PRESENTED TO THE FACULTY  
OF THE PRINCETON UNIVERSITY  
DEPARTMENT OF PHYSICS

ADVISED BY DR. MICHAEL JAWORSKI  
PRINCETON PLASMA PHYSICS LABORATORY

APRIL 30 2018

# Abstract

Artificially generated atmospheric pressure plasma arcs, with core temperatures on the order of 1 eV, are representative of conditions expected to occur within magnetohydrodynamic (MHD) generators, where arcs between the plasma and electrodes place stringent limitations on the lifetime of such systems. As such, a detailed analysis of these arcs is necessary for the construction of more sophisticated MHD converters. We describe the theory and implementation concerns of a near-resonance optical schlieren (NROS) diagnostic and a Fourier-transform infrared spectroscopy (FTIR) diagnostic for analyzing atmospheric plasma arcs. The FTIR and NROS diagnostics provide complementary information about arc composition and temperatures. They are additionally accompanied by predictive modeling performed using NASA's Chemical Equilibrium with Applications (CEA) program. Using the arc model and theoretical foundations of NROS, we develop a method for determining the ideal frequency to use in future NROS applications.

This paper represents my own work in accordance with University regulations.

# Acknowledgements

The author would like to call attention to the contributions of the following people, without whom this thesis would not exist:

- ★ First and foremost, my deepest thanks go to Dr. Mike Jaworski for his constant support, guidance, assistance, and patience over the course of this entire project, for introducing me to optical diagnostics in the first place, and for his wise counsel in all things plasma physics related.
- ★ Special thanks to Professor Sam Cohen, for introducing me to plasma physics and allowing me to explore experimental work in the field and providing sound academic and career advice over my years at Princeton.
- ★ Thanks to Professor Michael Romalis for agreeing to be my second reader.
- ★ Much love and eternal gratitude to Paige Kunkle, Emily Ho, George Kevrekidis, Charles Stahl, Chris Jagoe, Taylor Kulp-McDowall, Raheem Barnett, Nabai Habtemariam, and Akash Levy, who are the best damn friends anyone could ever ask for. Their unflagging emotional support and many late-night thesis sessions were instrumental in the writing of this work.
- ★ And of course, thanks to my parents and sister for always standing by my side and supporting me in my choices, even though they may have not always been the best ones.

# Contents

Abstract . . . . .	ii
Acknowledgements . . . . .	iii
List of Figures . . . . .	vi
<b>1 Introduction and Motivation</b>	<b>1</b>
1.1 Energy Conversion . . . . .	1
1.2 Optical Diagnostics . . . . .	4
<b>2 Theory</b>	<b>6</b>
2.1 Plasma Arcs . . . . .	6
2.1.1 Plasma . . . . .	7
2.1.2 Chemical Equilibrium . . . . .	8
2.1.3 The Elenbaas-Heller Equation . . . . .	9
2.2 Schlieren Photography . . . . .	14
2.3 Index of Refraction . . . . .	17
2.3.1 Doppler Broadening . . . . .	24
2.4 Fourier-Transform Infrared Spectroscopy . . . . .	29
2.5 Molecular Emission Spectra . . . . .	31
2.5.1 Rotational Spectra . . . . .	33
2.5.2 Vibrational Spectra . . . . .	38
2.5.3 Roto-Vibrational Spectra . . . . .	44
<b>3 Implementation Concerns</b>	<b>46</b>
3.1 Frequency Selection . . . . .	46
3.1.1 Determining an Appropriate Transition . . . . .	46
3.1.2 Frequency Detuning . . . . .	48
3.2 Obtaining $\rho(r)$ from $\epsilon(y)$ . . . . .	49
3.2.1 Abel Inversion . . . . .	50
3.3 Determining $\rho(r)$ from $n(r)$ . . . . .	52

3.4	Instrumentation Considerations . . . . .	53
3.5	Sample Coal Arc . . . . .	54
3.5.1	Quantitative Wavelength Selection . . . . .	59
3.6	FTIR and NROS, Together . . . . .	64
<b>4</b>	<b>Conclusion</b>	<b>66</b>
4.1	Future Directions . . . . .	67
	<b>Bibliography</b>	<b>69</b>
<b>A</b>	<b>Possible Instrumentation</b>	<b>71</b>
<b>B</b>	<b>Sample Arc Code Results</b>	<b>73</b>
<b>C</b>	<b>Plasma Arc Simulation Code</b>	<b>77</b>
<b>D</b>	<b>Index of Refraction Code</b>	<b>89</b>
<b>E</b>	<b>Ideal Wavelength Finder</b>	<b>93</b>

# List of Figures

1.1	Basic MHD generator schematic. . . . .	2
2.1	Simple schlieren system diagram . . . . .	14
2.2	Z-type schlieren system diagram . . . . .	16
2.3	Frequency dependence of $n$ and $a$ . . . . .	20
2.4	Index of refraction and absorption coefficient of lithium . . . . .	23
2.5	Effect of Doppler broadening on absorption coefficient . . . . .	26
2.6	Effect of Doppler broadening on index of refraction . . . . .	28
2.7	Schematic diagram of an FTIR detector system. . . . .	30
2.8	Energy level splitting in asymmetric top molecules . . . . .	37
2.9	Normal modes for an $XY_2$ bent molecule . . . . .	40
2.10	An example roto-vibrational spectrum . . . . .	44
3.1	Cartoon of the geometry of the arc system . . . . .	50
3.2	Temperature map in the sample arc. . . . .	55
3.3	Map of (neutral) potassium in the arc. . . . .	56
3.4	Absorption coefficient for wavelengths farther from resonance. . . . .	57
3.5	Absorption coefficient for wavelengths very near resonance. . . . .	58
3.6	Refractivity map for frequencies near resonance. . . . .	59
3.7	Detail of refractivity profiles. . . . .	60
3.8	Utility function for the sample coal arc. . . . .	63
A.1	Z-type schlieren diagram, for reference . . . . .	71

# Chapter 1

## Introduction and Motivation

### 1.1 Energy Conversion

Despite significant evidence linking coal and other carbon-burning power sources to climate change and other adverse environmental effects, modern energy technology continues to rely heavily on fossil fuels to fulfill the world's energy needs. For example, in 2016 the United States generated 64% of its electricity by burning either natural gas or coal [1]. Many research institutions, such as the Princeton Plasma Physics Laboratory (PPPL) and other Department of Energy (DOE) laboratories, aim to develop fully carbon-independent energy sources such as solar, wind, and nuclear power plants. Although much fruitful work has been done in developing these new energy sources, challenges remain: solar and wind power struggle to be scalable; fissile nuclear power plants produce dangerous byproducts and represent a nuclear proliferation risk; and fusion energy continues to await the necessary scientific advancements to make it possible. Furthermore, as long as the energy industry remains strongly dominated by coal and natural gas-burning power plants, the existence of

current infrastructure disincentivizes corporations from investing in new development, leaving the timescale for adopting newer technologies uncertain. Thus, it will be fruitful to develop energy conversion methods that mediate between existing infrastructure and clean energy, bridging the gap until newer technology can fully take precedence. To that end, we begin by considering one possible application of plasma physics to improving fossil fuel energy conversion; namely, magnetohydrodynamic (MHD) power generation.

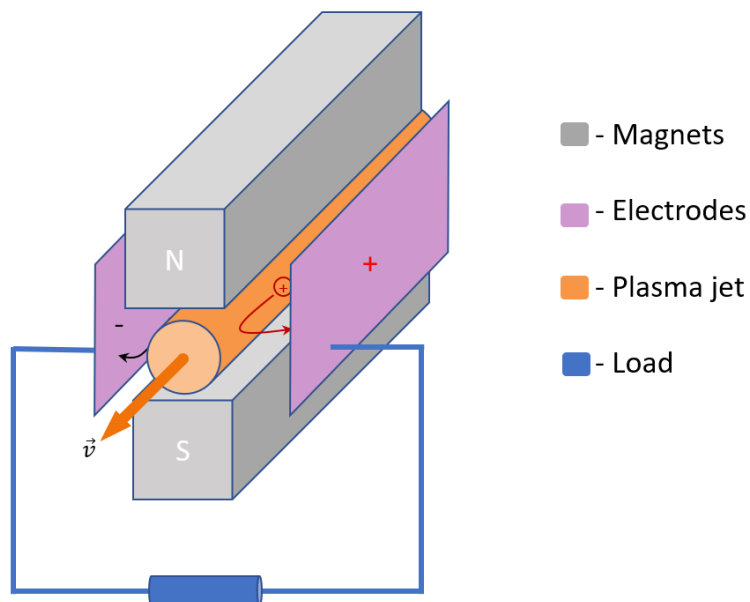


Figure 1.1: Basic MHD generator schematic.

Fossil fuel-burning power plants extract energy by boiling water and allowing the expanding steam to turn a turbine. Such systems contain a large number of moving parts and operate at relatively low temperatures, leaving room for improved efficiency. In contrast, MHD power converters contain no moving parts, and their



principle of operation necessitates a much higher operating temperature. As a result, it is comparatively easy to achieve high efficiency with MHD generators.

The principles behind their operation are quite straightforward: a fuel mixture is burned at a very high temperature, converting it into a plasma which is then forced through a region with a uniform magnetic field. On either side of this region are electrodes, as depicted in Fig. 1.1. The Lorentz force causes a potential difference to form across the two electrodes, in a direction perpendicular to the magnetic field and the flow velocity of the plasma. These can then be connected directly to provide power to the desired load, with no need for a moving turbine. Although this makes maximizing efficiency quite easy, modern MHD generators typically have efficiencies of about 20% [2]. However, advanced modern steam cycles achieve efficiencies of 40%; as a result, MHD generators alone are not a particularly attractive option. However, the exhaust temperature of the MHD systems is nearly as hot as the temperature of traditional coal flames used to boil water. Using an MHD generator as a topping cycle for a coal plant can increase the overall efficiency of a power plant by as much as 20 percentage points.

While they are theoretically capable of improving energy output significantly, the high operating temperature and working mechanism of the MHD generator also introduce unique engineering complications. As plasma-facing components, the electrodes in current MHD implementations suffer from large amounts of erosion caused by arcs from the plasma body. These arcs can be exceedingly hot, with core temperatures on the order of 1 eV ( $10^4$  K). As a result, MHD generator electrodes are known to decay almost entirely over the course of around 800 hours; for an economically

feasible one-year maintenance cycle, a lifetime of closer to 8000 hours is necessary [3]. In order to aid in the development of new electrodes, researchers require detailed diagnostics to help analyze atmospheric plasma arcs.

## 1.2 Optical Diagnostics

When analyzing plasmas, different diagnostics are appropriate for measuring different quantities. A variety of diagnostics that are physically inserted into the plasma body are capable of this analysis, including Langmuir probes, capacitive probes, ball-pen probes, and Faraday cups. One drawback of such methods is that they are, by nature, invasive; probes interacting with the plasma can disrupt it. Additionally, because they are exposed to a harsh environment their lifetime can suffer, depending on the temperature of the plasma in question. In an effort to avoid these effects, many plasma experiments instead use optical diagnostics, particularly interferometry and spectroscopy.

This thesis focuses on developing two such optical diagnostics; a near-resonance optical schlieren (NROS) laser system and a Fourier-transform infrared (FTIR) spectroscopy system. The basic operating principles of each are quite simple; the schlieren system works through differential deflection of light, while the FTIR system is a more straightforward application of interferometry and spectroscopy. The theory behind each of these systems will be explored fully in the next chapter, and some implementation concerns for such diagnostics in the third chapter.

FTIR diagnostics and their usage in plasma physics are already quite well-established, while NROS remains a largely unexplored possibility. The goal of this thesis is to provide a stronger framework for the ways in which FTIR and NROS can operate together, and in particular develop robust computational predictions for the conditions the NROS system can be expected to observe, as well as to develop a quantitative method for determining the proper way to use NROS to observe a plasma (we develop a diagnostic sensitivity/throughput-dependent metric for which wavelengths are best used to examine a given plasma arc).

# Chapter 2

## Theory

In this chapter, we outline the plasma physics theory relevant to the two diagnostics, as well as the atomic, molecular, and optical physics that comprise their measurement capabilities. This includes modeling of plasma arcs, the derivation of index of refraction and absorption coefficient, and the principles molecular spectroscopy, in addition to the operating fundamentals of both optical systems.

### 2.1 Plasma Arcs

In order to design diagnostic models for plasma arcs, it is necessary to develop a set of preliminary expectations for arc characteristics. In this experiment, computational modeling of plasma arcs was performed in order to predict these properties.

Simulation of plasma arcs relies on the understanding of gas composition within an arc and how it relates to energy flow through the arc column. The first of these properties is most easily probed under the assumption that the arc exists at chem-

ical equilibrium, while the second is analyzed through solutions to the power-flow differential equation within the arc.

### 2.1.1 Plasma

The discussion of plasma arcs necessarily hinges on a working understanding of plasma itself. In the simplest terms, plasma is a fluid state of matter that contains higher energy than a gas. As a gas is heated, atoms within it inherit more and more energy until eventually they are able to ionize and the gas becomes electrically conductive. As a result, the macroscopic behavior of a plasma will be dominated by the electromagnetic fields it produces and is subjected to.

There are three characteristics which define a plasma [4]. These are

1. The Debye length  $\lambda_D$  (a quantity which characterizes the degree to which electric charges in the plasma are screened) is much smaller than the bulk size of the plasma itself, so that electric charges are effectively screened.
2. The plasma parameter  $\Lambda$  is much greater than unity.  $\Lambda$  is defined in terms of the Debye length  $\lambda_D$  and the electron density  $\rho_e$  as  $\Lambda = 4\pi\rho_e\lambda_D^3$ . This quantity is thus strongly correlated with degree of ionization, and is particularly relevant to our discussion of plasma arcs.
3. The frequency of electron plasma oscillations (propagation of Langmuir waves) is much larger than the frequency of electron-neutral collisions within the plasma – that is, that electric interactions dominate over conventional gas kinetics.

Most nonexotic matter in the universe is in the plasma state, including the sun and all other stars, the interplanetary medium, the interstellar medium, the intergalactic medium, accretion disks around stars and stellar remnants, supernova remnants, and star-forming nebulae.

### 2.1.2 Chemical Equilibrium

Because the temperature of the plasma we seek to examine is relatively low, we determine its composition using plasma chemistry, through the use of chemical equilibrium. For a given chemical mixture, chemical equilibrium is the state in which the relative concentration of reactants and products does not change with time. Typically, chemical equilibrium is dynamic rather than static – that is, the rates of forward and backwards reactions are the same, rather than no reaction taking place. This consideration places constraints on the free energy of a system. The simplified arc model involves constant temperature and pressure at each equilibrium location, so in particular we must consider the Gibbs free energy  $G$ . In general,  $G = U + pV - TS$ , where  $U$  is the internal energy of the system,  $p$  is the pressure,  $V$  is the volume,  $T$  is the temperature, and  $S$  is the entropy. At chemical equilibrium, we have  $dG/dt = 0$ . Thus, at chemical equilibrium,  $G$  is minimized. In a closed system, this amounts to fulfilling the relation

$$dG = \sum_{j=1}^m \mu_j dN_j = 0 \quad (2.1)$$

subject to the constraint that

$$\sum_{j=1}^m a_{ij} N_j = b_i^0 \quad (2.2)$$

where  $\mu_j$  is the chemical potential for molecule  $j$ ,  $a_{ij}$  is the number of atoms of element  $i$  in molecule  $j$ , and  $b_i^0$  is the total number of atoms of element  $i$ .

This system of equations will yield to the method of Lagrange multipliers, although it is clear that the more complicated the gas mixture, the more involved this problem is to solve. Fortunately, software exists to solve such systems quickly and efficiently. Our modeling utilized Chemical Equilibrium with Applications (CEA) [5], a program written by NASA. CEA calculates the equilibrium properties of gas mixtures at a given temperature and pressure. Supplied with a list of species and a temperature/pressure combination to examine, the program performs the Gibbs energy minimization procedure described above and outputs a list of species concentrations in addition to calculating thermal transport properties, mixture molar mass, and other derived quantities. The program's efficiency allows for the simulation of complex fuel mixtures over a wide range of temperatures (typically failing only when temperatures become low enough for gas phases to condense).

### 2.1.3 The Elenbaas-Heller Equation

The theory behind determining plasma arc characteristics is strongly concentrated in an understanding of the Elenbaas-Heller equation, which is a power balance equation that arises from certain simplifying assumptions applied to the more widely-applicable DC positive column energy equation [6]. To begin, we have

$$\nabla \cdot \vec{q} + \nabla \cdot \left( p\vec{v} + \rho\vec{v} \left( e + \frac{v^2}{2} \right) \right) - \vec{j} \cdot \vec{E} + \nabla \cdot \vec{q}_{\text{rad}} = 0 \quad (2.3)$$

where  $\vec{q}$ ,  $p$ ,  $\vec{v}$ ,  $e$ ,  $\vec{j}$ ,  $\vec{E}$ , and  $\vec{q}_{\text{rad}}$  are the conductive flux, the pressure, the flow velocity, the enthalpy, the current density, the electric field, and the radiative flux, respectively. The first term in the equation is a conductive term; the second is a convective term; the third is a Joule heating term; and the last is a radiative loss term. The Elenbaas-Heller equation emerges under the following simplifying assumptions:

1. Convection is negligible (self-induced magnetic field is small).
2. Ohm's law ( $\vec{j} = \sigma \vec{E}$ , for electrical conductivity  $\sigma$  and electric field  $\vec{E}$ ) holds.
3. Gas flow in the arc itself is negligible ( $\vec{v} \approx 0$ ) over the time-scale of interest.
4.  $\nabla \cdot \vec{q}_{\text{rad}} = 4\pi\epsilon_N$ , where  $\epsilon_N$  is a net emission coefficient.
5. Heat conducts via the Fourier law,  $\vec{q} = -\kappa \nabla T$  (for thermal conductivity  $\kappa$ ).

When these conditions are applied to a long cylindrical arc, we obtain the Elenbaas-Heller equation in its usual form:

$$\sigma E^2 + \frac{1}{r} \frac{\partial}{\partial r} \left( \kappa r \frac{\partial T}{\partial r} \right) - 4\pi\epsilon_N = 0. \quad (2.4)$$

Gueye et al. [6] recommend reparameterizing this equation in terms of the heat flux potential  $S$ , which is the temperature integral of the thermal conductivity

$$S(T) = \int_{T_{\text{ref}}}^T \kappa(\tau) d\tau. \quad (2.5)$$



Under this transformation, the equation takes the form

$$E^2\sigma + \frac{1}{r}\frac{\partial}{\partial r}\left(r\frac{\partial S}{\partial r}\right) - 4\pi\epsilon_N = 0. \quad (2.6)$$

Solutions to the Elenbaas-Heller equation are not straightforward when the radiative loss term,  $4\pi\epsilon_N$ , is included, but when the current passed through an arc is low enough it is possible to neglect the power lost due to radiation ( $\epsilon_N = 0$ ). In this case, the solutions to the equation depend on the functional form of the electrical conductivity  $\sigma(S)$ . It is possible to calculate  $\sigma(T)$  (and thus  $\sigma(S)$ ) for a given gas composition as follows:

1. Calculate the total number density of particles, electrons, and neutrals at chemical equilibrium.
2. Calculate the values for the plasma parameter  $\Lambda$  and the Coulomb logarithm based on  $N_e$  and  $T$

$$\log_{10} \Lambda = \log_{10} \left( \frac{12\pi}{\sqrt{N_e}} \left( \frac{\varepsilon_0 k_B T}{q_e^2} \right)^{3/2} \right). \quad (2.7)$$

3. Calculate the ion collision term

$$\mathcal{I} = 3.9N_e \left( \frac{q_e^2}{8\pi\varepsilon_0 k_B T} \right)^2 \log_{10} \Lambda. \quad (2.8)$$

4. Calculate the neutral collision terms in terms of the momentum transfer cross sections  $\sigma_m$  (given by [7], [8], [9], [10], [11]):  $\mathcal{N} = \sum_i N_i \sigma_{mi}$

5. Use these values to calculate the electrical conductivity

$$\sigma = \sqrt{\frac{\pi}{8k_B T m_e}} \frac{N_e q_e^2}{\mathcal{N} + \mathcal{I}}. \quad (2.9)$$

6. Once the quantity  $\sigma(T)$  is known, invert  $S(T)$  as appropriate to obtain  $\sigma(S)$ .

The Elenbaas-Heller equation admits simple analytic solutions if the electrical conductivity can be fitted to a ramp function  $\mathcal{R}(x) = \max(x, 0)$  such that  $\sigma(S) = \mathcal{R}(\mathcal{B}(S - s_1))$  for constants  $\mathcal{B}$  and  $s_1$ . This corresponds to the arc channel having a region at the center where the electrical conductivity increases linearly as a function of heat flux, and an outer region, where the gas mixture is not conductive and the heat flux is lower. Based on the simulations performed, this approximation is reasonable for a variety of gas mixtures with varying complexities (see Appendix B). Its simplicity makes it ideal for gross predictive analysis of gas composition.

Under this approximation, for an infinitely long cylindrical channel of radius  $R$  the Elenbaas-Heller equation (with radiative term ignored) is then written as

$$E^2 \mathcal{B}(S - s_1) + \frac{1}{r} \frac{\partial}{\partial r} \left( r \frac{\partial S}{\partial r} \right) = 0 \quad \rho R < r < R \quad (2.10)$$

$$\frac{1}{r} \frac{\partial}{\partial r} \left( r \frac{\partial S}{\partial r} \right) = 0 \quad 0 < r < \rho R \quad (2.11)$$

where  $\rho R$  is the radius of the conducting part of the arc ( $0 < \rho < 1$ ). Boundary conditions for this equation are given by

1.  $S(\rho R) = s_1$  for both branches of the solution
2.  $S'(\rho R)^+ = S'(\rho R)^-$  (continuity of the first derivative at the boundary)

3.  $S(R) = s_2$  (the heat flux at the boundary, typically zero) and  $S'(R) = 0$

The equation with these boundary conditions admits the solution

$$S(r) = \begin{cases} s_1 - \frac{s_1 - s_2}{\beta J_1(\beta) \log \rho} J_0\left(\frac{\beta}{\rho R} r\right) & 0 < r < \rho R \\ s_1 + \frac{s_1 - s_2}{\log \rho} \log\left(\frac{r}{\rho R}\right) & \rho R < r < R \\ 0 & r > R \end{cases} \quad (2.12)$$

where  $\rho$  depends on the electric field and  $\beta$  is the first zero of  $J_0(x)$ . Using Ohm's law to write  $\rho$  in terms of the applied current, we have the condition

$$\frac{\rho}{\log(1/\rho)} = \frac{\beta I}{2\pi(s_1 - s_2)\sqrt{\mathcal{B}R}}. \quad (2.13)$$

Solving for  $\rho(I)$  using the Lambert  $W$ -function yields the solution

$$\rho(I) = \frac{\beta}{2\pi(s_1 - s_2)\sqrt{\mathcal{B}R}} I W\left(\frac{2\pi(s_1 - s_2)\sqrt{\mathcal{B}R}}{\beta I}\right). \quad (2.14)$$

These equations, in conjunction with Ohm's law, allow us to calculate any desired properties of the arc, including axis temperatures, arc radii, and power flow (IV curves) as functions of current, along with arc composition – see Appendix B for examples of such data for a sample coal-burning arc.

## 2.2 Schlieren Photography

Having concluded our theoretical and computational discussion of plasma arcs, we turn to the discussion of schlieren photography and its applications to the construction of diagnostic instruments.

On a basic level, schlieren photography is very simple. Incoming light is directed through a region with nonuniform index of refraction, such as a plasma arc, and then focused using a lens or mirror onto a knife edge cutoff, behind which lies a detector system.

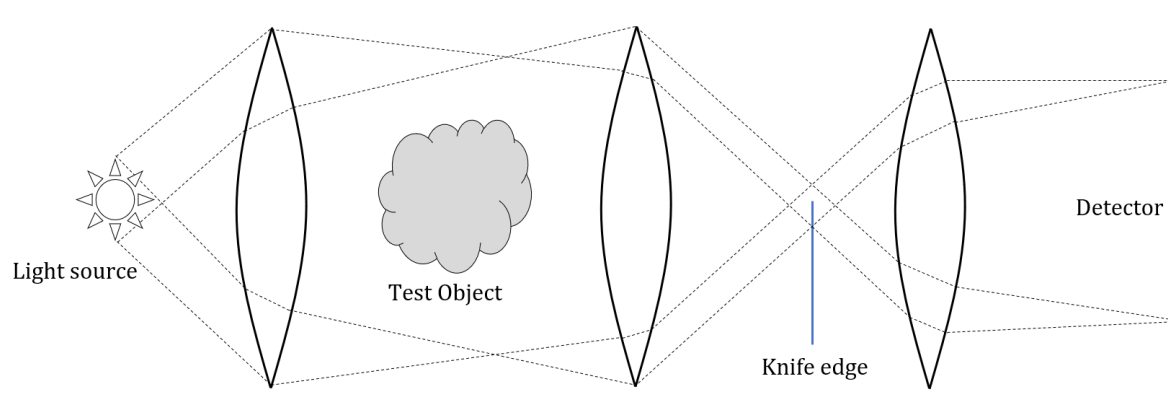


Figure 2.1: A simple lens-based schlieren system with relevant parts labelled. Adapted from a figure in [12].

In the absence of a test object, some portion of the original light arrives and uniformly illuminates the detector screen, resulting in a flat image. Imaging of a test object occurs because the nonuniform refractive index causes some rays of light that would originally hit the knife edge (and not reach the detector) to pass the knife edge and brighten the screen, and vice-versa for some rays that would originally

pass through the knife edge. Thus, the resulting image will have areas of varying brightness depending on the distribution of the refractive index.

In particular, the bright regions will depend on the first derivative of the refractive index. To see why this is the case, one must consider the deflection of a beam of light moving through a region with nonuniform refractive index. [12] gives that the curvature of the light ray is given by

$$\frac{\partial^2 x}{\partial z^2} = \frac{1}{n} \frac{\partial n}{\partial x} \quad \text{and} \quad \frac{\partial^2 y}{\partial z^2} = \frac{1}{n} \frac{\partial n}{\partial y} \quad (2.15)$$

where  $z$  is the optical axis and  $n(x, y)$  is the refractive index in the coordinates perpendicular to the axis (note that the schlieren system will not detect an index of refraction that varies only in  $z$ , so the object has to be oriented the right way). Therefore, the angular deflection in each direction is given by the  $z$ -integral of these curvatures;

$$\epsilon_x = \int \frac{1}{n} \frac{\partial n}{\partial x} dz \quad \text{and} \quad \epsilon_y = \int \frac{1}{n} \frac{\partial n}{\partial y} dz \quad (2.16)$$

and because the intensity of the output image is linearly proportional to the deflection, it is clear that the schlieren system is able to directly measure the first spatial derivatives of the index of refraction.

The schematic shown in Fig. 2.1 illustrates the general principles for a schlieren system, but does not necessarily make for the most effective actual schlieren design. The MHD generator project already makes use of a two-color schlieren system from which the tunable system will evolve directly; it is based on the  $Z$ -type mirror-based

schlieren system outlined in [12]. A schematic diagram for the Z-type system is given below.

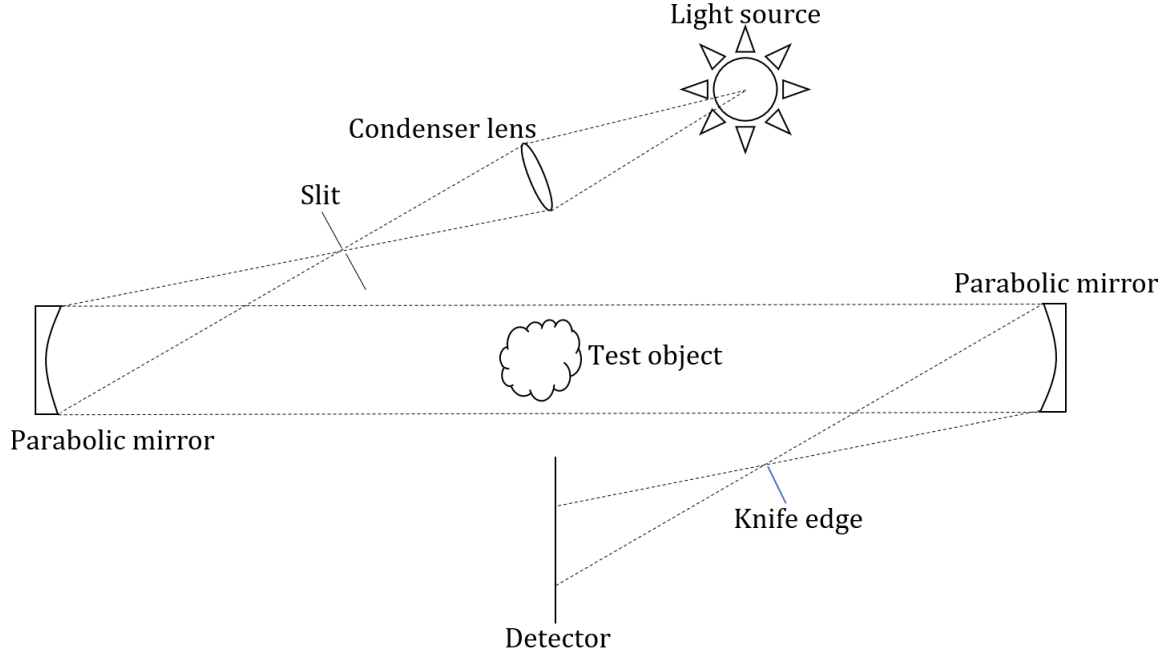


Figure 2.2: The basic Z-type schlieren system that we propose to use for the NROS system. The current two-color system is very similar, but slightly adapted to accommodate two lasers. Adapted from a figure in [12].

In the case of the NROS system, the test object will be a cylindrical arc system whose circular cross section would correspond to the cloudy plasma depicted in the figure. It is worth noting that this orientation of mirrors is particularly effective, compared to that where the source and detector are both on the same side of the optical axis; because the parabolic mirrors are angled oppositely, the coma that results from a single mirror is canceled out by the other. In the other system, the coma would double after the pass through the second mirror.

[12] also gives definitions for the contrast and the sensitivity of the schlieren system for a  $Z$ -type arrangement. The contrast of the schlieren image  $C$  is given by

$$C = \frac{f_2 \epsilon_y}{a} = \frac{f_2}{a} \int \frac{1}{n} \frac{\partial n}{\partial y} dz \quad (2.17)$$

where  $f_2$  is the focal length of the second mirror,  $\epsilon_y$  is the angular deflection in the  $y$ -direction<sup>1</sup>, and  $a$  is the height of the undeflected image on the detector screen (the part that makes it over the knife edge, a quantity which can be adjusted by moving the knife edge). A greater contrast will result from a larger deflection, and thus from a larger index of refraction change – this is the crux of the operation of the NROS system. As an aside, the sensitivity is defined as the  $\epsilon$ -derivative of the contrast, giving  $S = f_2/a$ .

## 2.3 Index of Refraction

As the discussion of schlieren photography makes clear, a detailed analysis of index of refraction is critical for constructing schlieren diagnostics. As it turns out, it is also of the utmost importance for understanding the NROS diagnostic. Here we outline the electrodynamic theory that allows the tunable schlieren system to achieve superior results to the general schlieren system outlined in the previous section. The key to improving sensitivity lies in the frequency-dependent nature of the index of refraction. Macroscopic geometric optics and introductory electromagnetism courses present the index of refraction as being constant in a given medium, defined in terms

---

<sup>1</sup>Note that rotating the knife-edge 90° will measure deflections in  $x$  instead.

of the permittivity  $\varepsilon$  and permeability  $\mu$  as

$$n = \sqrt{\frac{\mu_0 \varepsilon_0}{\mu \varepsilon}} = \frac{c}{v} \quad (2.18)$$

where  $v$  is the phase velocity of light in the medium. Additionally, the Gladstone-Dale law ( $n = 1 + k_g \rho$  where  $k_g$  is the Gladstone-Dale coefficient of the gas) gives the index of refraction as a function of the gas concentration  $\rho$ . These two definitions are critical for the analysis of a non-resonant schlieren system. However, a more detailed microscopic analysis reveals the well-known fact that the index of refraction  $n$  behaves rather differently when the incident radiation carries energy near that of an electronic transition, resulting in a frequency- and density-dependent index  $n(\rho, \omega)$ .

We take a classical approach to the electromagnetic interaction as outlined in [13]. Suppose the incident light is monochromatic with polarization  $\hat{\varepsilon}$ . Then in the dipole approximation the incident electric field is<sup>2</sup>

$$\mathbf{E}^+(t) = \hat{\varepsilon} E_0 e^{-i\omega t}. \quad (2.19)$$

Then the force felt by an electron by this field is given by  $\mathbf{F}^+ = -q_e \mathbf{E}^+$ . A physically reasonable approximation is to treat the motion of the electron as that of a driven damped harmonic oscillator;

$$m_e \ddot{\mathbf{x}}^+ + m_e \gamma \dot{\mathbf{x}}^+ + m_e \omega_0^2 \mathbf{x}^+ = -q_e \hat{\varepsilon} E_0 e^{-i\omega t} \quad (2.20)$$

---

<sup>2</sup>The physically realizable field  $\mathbf{E}$  is the sum of a positive frequency part and a negative frequency part; for convenience we work only with the positive frequency part, but both are physically significant:  $\mathbf{E}(t) = 2 \operatorname{Re}\{\mathbf{E}^+(t)\}$ . This convention continues for the remainder of the section.



Qualitatively, this makes sense; the restoring force of the nuclear charge is the linear term of the equation of motion, while the damping term arises from loss of energy due to phenomena such as Larmor radiation<sup>3</sup>. This ODE admits a familiar solution of the form  $\mathbf{x} = \hat{\varepsilon}x_0e^{-i\omega t}$ , where analysis of the initial conditions reveals

$$x_0 = \frac{q_e E_0}{m_e(\omega^2 - \omega_0^2 + i\gamma\omega)}. \quad (2.21)$$

Then if the dipole moment of the atom is  $\mathbf{p}^+ = -q_e\mathbf{x}^+ \equiv \alpha(\omega)\mathbf{E}^+$ , then the polarizability  $\alpha$  is given for the damped case is

$$\alpha(\omega) = \frac{q_e^2}{m_e(\omega_0^2 - \omega^2 - i\gamma\omega)}. \quad (2.22)$$

Meanwhile, the susceptibility  $\chi(\omega)$  is given by

$$\begin{aligned} \chi(\omega) &= \frac{\rho}{\varepsilon_0}\alpha(\omega) = \frac{\rho q_e^2}{m_e \varepsilon_0(\omega_0^2 - \omega^2 - i\gamma\omega)} \\ &= \frac{\rho q_e^2}{m_e \varepsilon_0} \left( \frac{\omega_0^2 - \omega^2}{(\omega_0^2 - \omega^2)^2 + \gamma^2\omega^2} + i \frac{\gamma\omega}{(\omega_0^2 - \omega^2)^2 + \gamma^2\omega^2} \right). \end{aligned} \quad (2.23)$$

where in the second step we have separated the real and imaginary parts in the usual manner. If  $\chi(\omega)$  is small, which it typically is, the complex index of refraction is then given by the relation  $\tilde{n} = \sqrt{1 + \chi} \approx 1 + \chi/2$  and we have

$$\tilde{n} \approx 1 + \frac{\rho q_e^2}{2m_e \varepsilon_0} \left( \frac{\omega_0^2 - \omega^2}{(\omega_0^2 - \omega^2)^2 + \gamma^2\omega^2} \right) + i \frac{\rho q_e^2}{2m_e \varepsilon_0} \left( \frac{\gamma\omega}{(\omega_0^2 - \omega^2)^2 + \gamma^2\omega^2} \right) \quad (2.24)$$

---

<sup>3</sup>Actual values for  $\gamma$  are experimentally determined; more on this later.

An electromagnetic wave propagates in space as  $E = E_0 \exp(ik_0 \tilde{n}z)$ . Thus, from the complex index of refraction we can immediately read off the classical index of refraction  $n(\omega)$  and the classical absorption coefficient  $a(\omega)$  (also called extinction coefficient; intensity  $I(z) = I_0 e^{-az}$ ). The real part of  $\tilde{n}(\omega)$  gives rise to the phase shift corresponding to the index of refraction, while the imaginary part gives rise to exponential decay in space corresponding to the absorption coefficient. We have

$$n(\omega) = \text{Re}\{\tilde{n}(\omega)\} = 1 + \frac{\rho q_e^2}{2m_e \varepsilon_0} \left( \frac{\omega_0^2 - \omega^2}{(\omega_0^2 - \omega^2)^2 + \gamma^2 \omega^2} \right) \equiv 1 + \frac{\rho q_e^2}{2m_e \varepsilon_0} \xi(\omega) \quad (2.25)$$

$$a(\omega) = 2k_0 \text{Im}\{\tilde{n}(\omega)\} = \frac{2\omega}{c} \text{Im}\{\tilde{n}(\omega)\} = \frac{\rho q_e^2}{m_e \varepsilon_0 c} \left( \frac{\gamma \omega^2}{(\omega_0^2 - \omega^2)^2 + \gamma^2 \omega^2} \right). \quad (2.26)$$

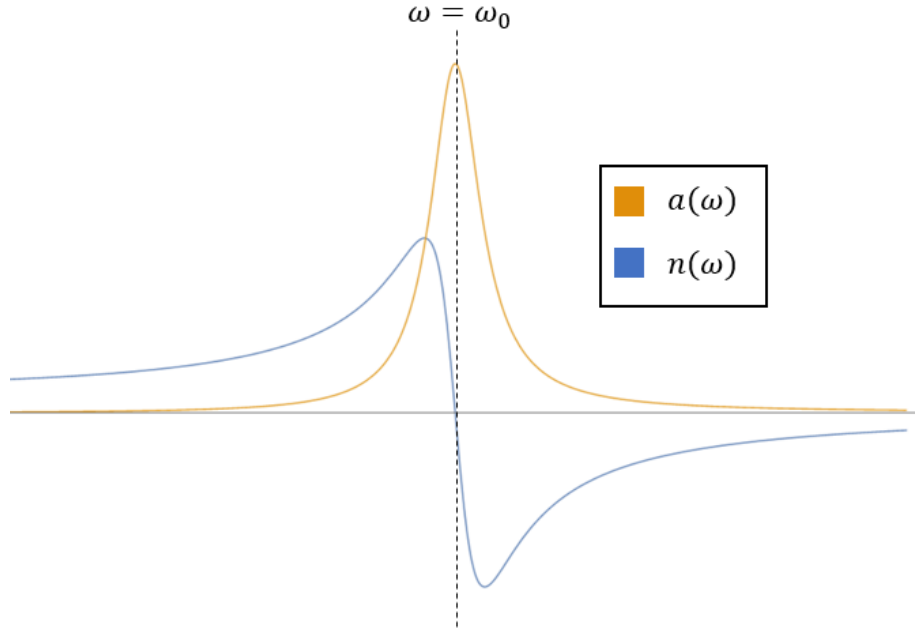


Figure 2.3: Qualitative behavior of  $n(\omega)$  and  $a(\omega)$  near a resonance at  $\omega_0$  – for realistic atoms the peaks are much sharper.

It is also important to consider the possibility of multiple electronic transitions, as most atoms have multiple electrons. It is straightforward to generalize the development above to such atoms; simply sum over all the available transitions. Thus, the susceptibility is

$$\chi(\omega) = \frac{\rho q_e^2}{m_e \varepsilon_0} \sum_k \frac{f_{0k}}{(\omega_{0k}^2 - \omega^2 - i\gamma_k \omega^2)} \quad (2.27)$$

where  $f_{0k}$  is the oscillator strength; from a quantum mechanical perspective, this corresponds to the probability of an electron making a transition from the ground state energy to the  $k$ -th energy level. That is to say, each term in the sum corresponds to the possibility of an electron transitioning to a different excited state. The index of refraction and absorption coefficient change appropriately:

$$n(\omega) = 1 + \frac{\rho q_e^2}{2m_e \varepsilon_0} \sum_k \frac{(\omega_{0k}^2 - \omega^2) f_{0k}}{(\omega_{0k}^2 - \omega^2)^2 + \gamma_k^2 \omega^2} \quad (2.28)$$

$$a(\omega) = \frac{\rho q_e^2}{m_e \varepsilon_0 c} \sum_k \frac{\gamma_k \omega^2 f_{0k}}{(\omega_{0k}^2 - \omega^2)^2 + \gamma_k^2 \omega^2}. \quad (2.29)$$

It is worth noting at this point the relationship between the oscillator strengths  $f_{0k}$  and damping parameters  $\gamma_k$ . In the quantum mechanical treatment, the damping parameter  $\gamma_k$  is equivalent to the Einstein A coefficient  $A_{k1}$  and encodes information about the lifetime of the excited state. Additionally, [13] gives the fully quantum-mechanical value for the absorption cross section  $\sigma$  (defined as  $\sigma(\omega) = a(\omega)/\rho$ ) at resonance as

$$\sigma(\omega_0) = \frac{\lambda_{0k}^2}{2\pi} = \frac{2\pi c^2}{\omega_{0k}^2} \quad (2.30)$$

while the classical treatment resulted in

$$\sigma_c(\omega_0) = \frac{e^2}{m_e \varepsilon_0 c \gamma_k}. \quad (2.31)$$

The quantum mechanical treatment, obviously, is the one that is quantitatively correct; the oscillator strength, then, is defined as a correction to the classical result so that  $f_{0k} = \sigma/\sigma_c$ . Taking into account degeneracy of energy levels, we have

$$f_{0k} = \frac{2\pi\varepsilon_0 m_e c^3 \gamma_k}{q_e^2 \omega_{0k}} \frac{g_k}{g_0} \quad (2.32)$$

where  $g_k$  is the degeneracy of the  $k$ -th energy level. This equation allows us to calculate values for oscillator strengths from values of  $\gamma_k$ , which are exhaustively tabulated (though often recorded as Einstein coefficients instead.)

In practice, it is frequently necessary to consider the presence of multiple transitions near a given frequency because electronic energy levels are in general not degenerate in total angular momentum  $j$ . For example, lithium ( $Z = 3$ ) and potassium ( $Z = 19$ ) are both of interest to plasma applications and have ground-state transitions in regions probeable by visible frequency lasers. Both species also have a second transition very close to the first (for lithium, one at 670.776 nm and one at 670.791 nm; and for potassium one at 404.414 nm and one at 404.720 nm [14]); the two peaks correspond to the upper energy level having  $j = 1/2$  or  $j = 3/2$ . Owing to their closeness, these transitions also have values for  $f_{0k}$  which are of the same order of magnitude, and so both must be considered when calculating  $\chi(\omega)$  and its derived quantities.

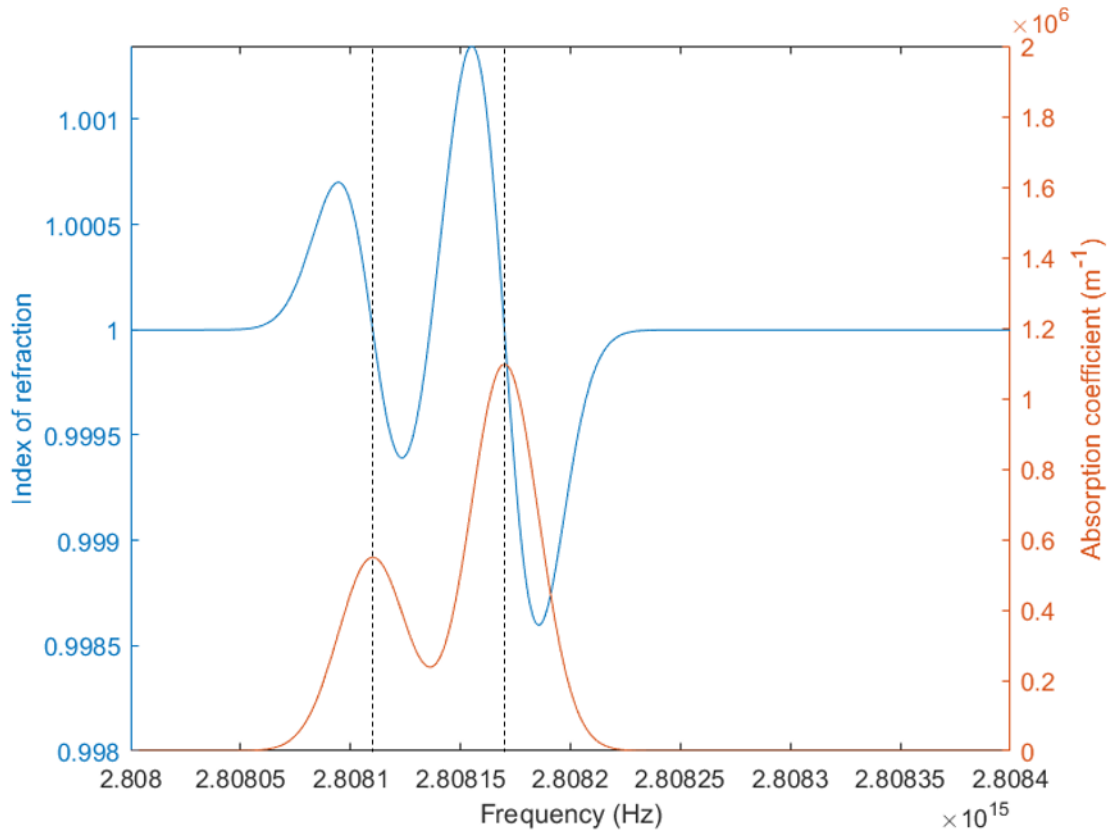


Figure 2.4: Index of refraction and absorption coefficient in a lithium gas near the double peak, with approximate Doppler correction ( $\delta$ -function approximation – see 2.4.1) performed.

This is not to say that a single transition is never found; for some species, transitions are far enough apart in frequency space that the frequency response near a particular resonance varies only as a result of the contribution from one transition, as the frequency dependence for either  $n$  or  $a$  quickly falls to zero away from resonance. For others, one of the transitions will be forbidden by electric dipole selection rules and thus will be much less probable; such is the case with beryllium ( $Z = 4$ )

which has transitions at 454.805 nm and 454.854 nm, the first of which is a magnetic quadrupole transition and occurs roughly 1000 times less frequently [14].

### 2.3.1 Doppler Broadening

The above calculations only take into account the fact that the spectral lines are *naturally* broadened, and have a Lorentzian profile. This assumes no thermal motion of the atoms in question, which (particularly for a plasma) is a phenomenally optimistic assumption. In reality, some thermal motion will be present and the Doppler shift caused by this motion will cause a further broadening of the spectral lines and thus the profiles for the index of refraction and absorption coefficient.

As a result of thermal motion, a given atomic species will be moving either away from or towards the light source. Letting  $v$  be the velocity directed towards the source, then the atoms will observe the incident light not as having a frequency of  $\omega$ , but rather the blueshifted

$$\omega_D = \omega \left( 1 - \frac{v}{c} \right). \quad (2.33)$$

This equation also properly calculates the redshift for atoms moving away from the source, which will have  $v < 0$ . In order to obtain a properly broadened quantity, it is necessary to multiply the Doppler-shifted quantity by the fraction of atoms moving at that velocity, then integrate over all possible velocities. Thus, if there is some frequency-dependent quantity  $q(\omega)$ , the Doppler-corrected quantity associated with it will be given by

$$q_D(\omega) = \int_{-\infty}^{\infty} q \left( \omega - \frac{\omega v}{c} \right) f(v) dv \quad (2.34)$$

where  $f(v)$  is the probability distribution for the velocities in question. For pure thermal motion,  $f(v)$  will be a pure Maxwellian distribution. Because we are concerned only with the projection of velocity along the optical axis, the distribution will be the Gaussian [15]

$$f(v)dv = \frac{1}{\sqrt{\pi}} \sqrt{\frac{m}{2k_B T}} \exp\left(\frac{-mv^2}{2k_B T}\right) dv \quad (2.35)$$

which has an associated width of  $\Delta v = \sqrt{2k_B T/m}$ . We can convert this into a width in frequency-space:

$$\Delta\omega = \omega_0 \frac{\Delta v}{c} = \frac{\omega_0}{c} \sqrt{\frac{2k_B T}{m}}. \quad (2.36)$$

Changing the variable of integration via the substitution  $\Omega = \omega v/c$ , we can get the broadened quantity by writing the convolution in Eq. 2.34 [16]

$$q_D(\omega) = \frac{1}{\sqrt{\pi}\Delta\omega} \int_0^\infty q(\omega - \Omega) \exp\left(-\left(\frac{\Omega}{\Delta\omega}\right)^2\right) d\Omega \quad (2.37)$$

so the Doppler broadening amounts to convolving the function with a Gaussian. For the exact form of  $n(\omega)$  and  $a(\omega)$ , initial attempts to compute realistic line widths revealed that this convolution is very computationally costly, representing over 95% of the time required to produce profiles for index of refraction and absorption coefficient. As such, we seek approximation methods.

For the absorption coefficient, the profile is Lorentzian and the convolution of a Lorentzian and a Gaussian is known to be a Voigt profile. One possible method for approximating the Voigt profile is to use a linear combination of the Lorentzian and

the Gaussian rather than their convolution. However, this method does not work for the index of refraction, which is the primary quantity of interest.

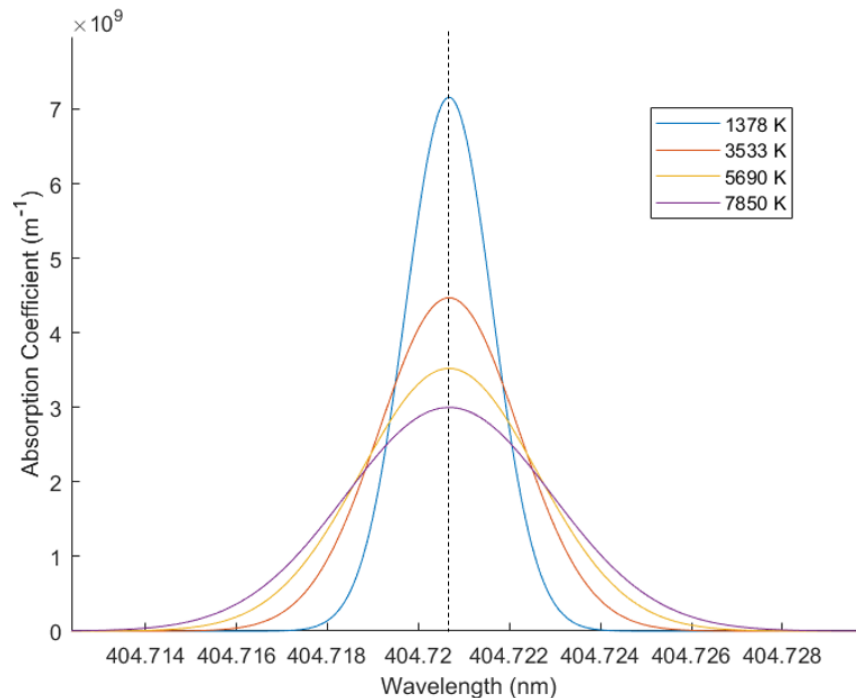


Figure 2.5: Example Doppler-broadened absorption coefficients for a very dense sample of potassium at various temperatures between 300 and 10000 K.

[16] suggest a different method for approximating the broadened  $a(\omega)$  profile, which we propose also works for the index of refraction profile with some small modifications. The method hinges on the fact that the width of the Lorentzian which results from natural broadening is much smaller than the width of the Gaussian which results from Doppler broadening: in terms of the symbols used in this text,  $\gamma_k \ll \Delta\omega$ . As a result, especially when we are interested in a broad range of frequencies we can approximate  $a(\omega)$  as a Dirac delta function  $\tilde{a}(\omega)$  with the same magnitude as the



absorption peak:

$$\tilde{a}(\omega) = a(\omega_0)\delta(\omega - \omega_0) \quad (2.38)$$

The convolution of a delta function is trivial to perform, and thus the absorption coefficient will have a broadened profile  $a_D(\omega)$  written as

$$a_D(\omega) = \frac{a(\omega_0)}{\sqrt{\pi}\Delta\omega} \exp\left(-\left(\frac{\omega - \omega_0}{\Delta\omega}\right)^2\right) \quad (2.39)$$

and of course we can sum over multiple peaks as necessary to obtain the full absorption profile when multiple transitions are present.

For preliminary calculations we propose modifying this method to apply the Doppler broadening effect to the index of refraction profile, although it is not immediately applicable. Considering just a single peak, we have that the index of refraction profile has two symmetrical peaks oddly distributed about the  $\omega = \omega_0$  axis, centered at  $\omega_{\mp} = \sqrt{\omega_0^2 \pm \omega_0\gamma}$ .<sup>4</sup> Although the profile is not a Lorentzian as is the case for the absorption coefficient, the two peaks still have characteristic width determined by the damping coefficient  $\gamma$ ; and once again, for the temperature regime of interest we have  $\gamma_k \ll \Delta\omega$ . Therefore, following the example for  $\tilde{a}(\omega)$  we propose decomposing the frequency dependence near resonance as

$$\tilde{\eta}(\omega) = \eta(\omega_-)\delta(\omega - \omega_-) + \eta(\omega_+)\delta(\omega - \omega_+) \quad (2.40)$$

---

<sup>4</sup>We choose this sign convention for  $\omega_{\mp}$  because the peak with positive magnitude occurs at the lower frequency.

where  $\eta(\omega) = n(\omega) - 1$ , noting that  $\eta(\omega_+) < 0$ . This results in a Doppler-broadened profile of the form

$$\eta_D(\omega) = \frac{1}{\sqrt{\pi}\Delta\omega} \left( \eta(\omega_-) \exp \left( -\left( \frac{\omega - \omega_-}{\Delta\omega} \right)^2 \right) + \eta(\omega_+) \exp \left( -\left( \frac{\omega - \omega_+}{\Delta\omega} \right)^2 \right) \right)$$

and the Doppler broadened index of refraction will be given by  $n_D(\omega) = 1 + \eta_D(\omega)$ . As in the case with the absorption coefficient, this equation can be easily modified to allow summation over several transitions.

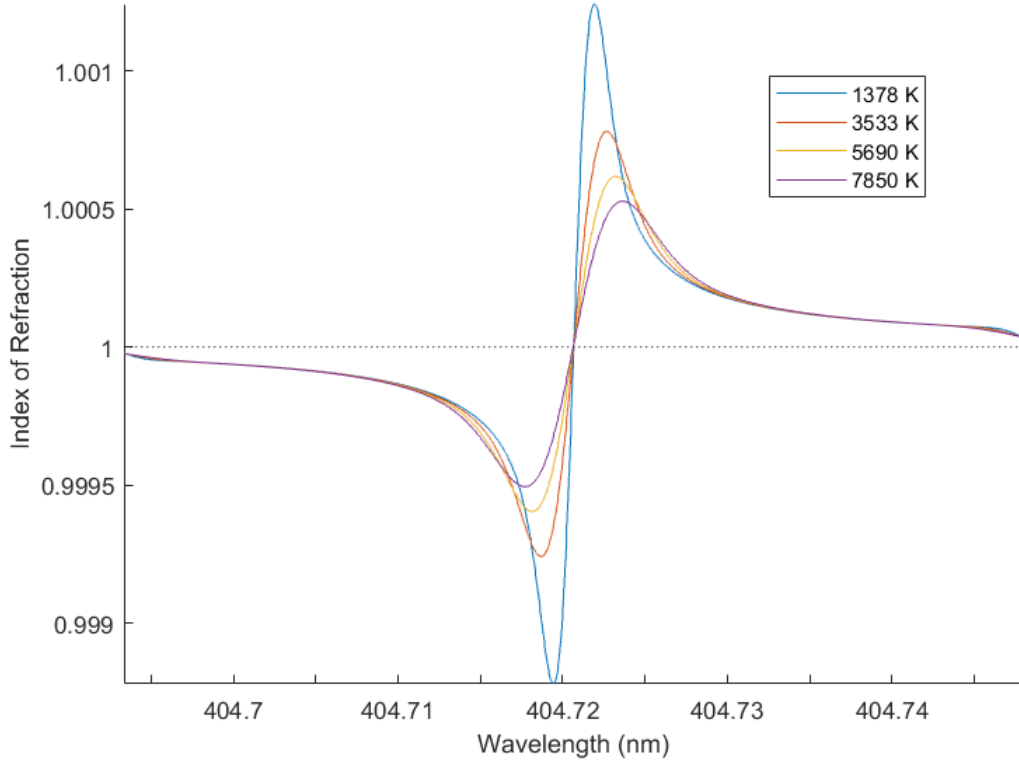


Figure 2.6: Example Doppler-broadened indices of refraction for the same sample of potassium as Fig. 2.5 across a range of temperatures.

The veracity of this delta function approximation is yet to be fully determined, and will likely await experimental tests that are beyond the temporal scope of this thesis. Nonetheless, preliminary results match the qualitative behavior of both broadened index of refraction and absorption coefficient profiles given by other authors, and we expect the approximation to be reasonably robust for preliminary calculations. Naturally, for actual implementation the full convolution will likely be more useful, despite its more demanding computational requirements. Since our initial calculations do not represent a major computational endeavour, in the next chapter we make use of Matlab’s built-in convolution function. These example calculations on both unbroadened index of refraction and the broadening model are performed in section 3.5 where we predict the index of refraction profile for a coal-burning plasma arc near the resonances of neutral potassium.

## 2.4 Fourier-Transform Infrared Spectroscopy

Compared to schlieren photography, Fourier-transform infrared (FTIR) spectroscopy is a very straightforward way to probe the structure of a plasma sample. Rather than relying on the index of refraction to obtain information about species concentrations, FTIR spectroscopy measures absorption to infer a spectrum from which relative line intensities will yield information about plasma composition. The most straightforward kind of infrared spectroscopy is known as *dispersive* spectroscopy, and it involves shining monochromatic light onto a sample, measuring absorption, then moving on to a different wavelength. FTIR spectroscopy operates in a simi-

lar way, but involves illuminating the sample with light containing many different wavelengths, measuring absorption, then repeating with light containing a different combination of wavelengths.

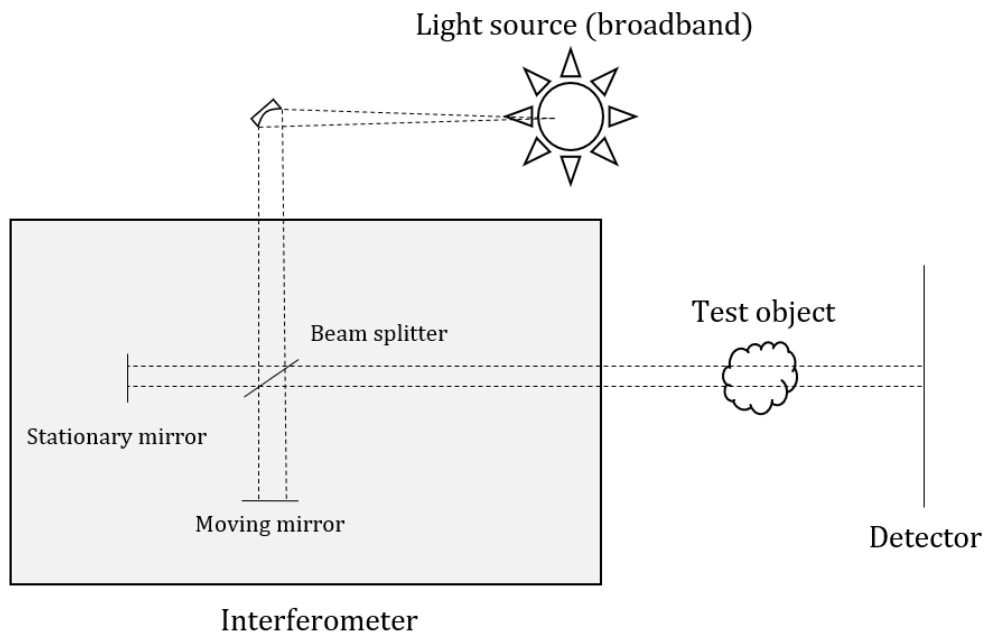


Figure 2.7: Schematic diagram of an FTIR detector system.

The light from the source is first passed through a Michelson interferometer, where optical path differences result in differential constructive/destructive interference depending on wavelength. The beam is then recombined, passed through the sample, and read by a detector, which results in a raw data sample known as an interferogram. The interferogram contains information about the relative intensities of the various wavelengths emitted from the broadband source. Finally, a Fourier transform is performed on the interferogram to obtain a spectrum, giving the diagnostic its name. In order to obtain the spectrum of the sample alone, the spectrum

must be deconvolved using the spectrum of the source without a sample; in practice, using commercial FTIR systems, this analysis is all done automatically. FTIR spectroscopy has a number of advantages over traditional dispersive spectroscopy; the most important are enumerated below [17]

1. Multiplex advantage: because data for all wavelengths are collected simultaneously, the system has a higher signal-to-noise ratio for a given observation time.
2. Throughput advantage: in a dispersive interferometer, slits are required which reduce the light that can pass through the sample. FTIR systems do not require such slits, and thus have higher throughput.
3. Wavelength accuracy: in FTIR, wavelength is calibrated by using a laser of a known wavelength in the interferometer system, while in dispersive systems physical movement of diffraction gratings sets the wavelength scale.

## 2.5 Molecular Emission Spectra

We turn now to the discussion of molecular emission spectra in the context of our two optical diagnostics. Both the NROS and FTIR systems rely on the underlying principles of spectroscopy: in the NROS system, the laser frequency must be tuned to a value near that of a particular emission line (although, for reasons we will discuss later, for the NROS specifically it will generally be preferable to use atomic rather than molecular emission lines); and in the FTIR system the device measures

emission lines directly. Naturally, the FTIR system can measure infrared-region transitions for atomic species. But because the plasma arcs being examined are composed primarily of polyatomic molecules in the temperature regime in question, instead of examining only atomic spectra we must also consider the considerably more complicated physics behind molecular spectra. A rich and expansive body of literature exists examining these phenomena; here we discuss the basic physics in order to understand the measurements that the FTIR system will yield. Much of the discussion is based on the exposition in Herzberg et al [18].

All molecules and atoms have electronic emission spectra whose energy levels are determined by quantized electron orbitals; for instance, for hydrogen the energies are given by the familiar Rydberg formula: where the electron mass is  $m_e$ , the fundamental charge is  $q_e$ , and the principal quantum number is  $n$  we have that the  $n$ -th energy level  $E_n$  is

$$E_n = -\frac{m_e q_e^4}{32\pi^2 \hbar^2 \epsilon_0^3 n^2}. \quad (2.41)$$

In addition to their electronic energy transitions, molecules also exhibit emission based on their rotational and vibrational energies. It is customary to split the total energy into the sum of electronic, rotational, and vibrational energies. This approximation works well so long as the energies of each interaction are well-separated; for diatomic molecules in particular this approximation is quite robust [18]. In polyatomic molecules, vibrational and rotational energy levels tend to be of a similar order and mutual interactions between the three kinds of motion render this approximation less accurate, though still suitable for most molecules. On the whole,

electronic transitions have higher energy than rotational and vibrational transitions, which tend to be in the infrared regime.

### 2.5.1 Rotational Spectra

In all cases, we may decouple the total wavefunction into electronic, rotational, and vibrational parts as  $\psi = \psi_e \psi_v \psi_r$  to decent approximation. In this section, we examine the eigenvalues of  $\psi_r$ , called rotational energy levels, for the different molecular geometries. Polyatomic molecules acquire different 3-dimensional geometries based on their atomic content according to the rules of valence shell electron pair repulsion (VSEPR) theory. The geometry a molecule adopts determines its rotational spectrum through its three principle moments of inertia. Molecules are classified by the relation between these moments. There are four such classifications: linear, spherical top, symmetric top, and asymmetric top.

#### Linear Molecules and Spherical Tops

Linear molecules have one very small moment of inertia and two larger, equal moments of inertia ( $I_A \approx 0$  and  $I_B = I_C$ ). Some examples of linear molecules include HCN and CO<sub>2</sub>. The nonzero moment  $I_B$  is calculated about an axis through the center of mass and perpendicular to the internuclear axis. In this case, the energy levels are given by

$$E_J = \frac{\hbar^2}{2I_B} J(J+1) - DJ^2(J+1)^2 + \dots \quad (2.42)$$

where the energies are indexed by  $J \in \mathbb{N}$ , the so-called rotational quantum number. The first term arises directly from the rotation of the molecule, while the second (quadratic) term is typically much smaller and arises from the non-rigidity of the molecule (internuclear separation increases slightly when a molecule is rotating as a result of centrifugal forces). In the harmonic oscillator approximation, regardless of the exact form of the molecule,  $D \propto I_B^{-3}$ , where the proportionality constant varies depending on molecular formula. The magnitude of the angular momentum vector is  $L = \hbar\sqrt{J(J+1)}$ . A particular property of linear molecules is that the total eigenfunction changes sign under reflection of all particles about the origin for odd values of  $J$  (these are called negative rotational levels), and remains the same for even values of  $J$  (positive rotational levels). Selection rules dictate that (electric dipole) transitions can only occur for molecules that have a permanent dipole moment; can only occur between positive and negative rotational levels; and have  $\Delta J = \pm 1$ . This results in nearly evenly-spaced peaks in frequency space.

Spherical top molecules have all three moments of inertia equal ( $I_A = I_B = I_C$ ). Due to the high degree of symmetry, spherical top molecules exhibit the same energy level structure as linear molecules. However, if all three moments of inertia are equal then a molecule cannot have a permanent dipole moment, meaning no electronic transitions will be allowed; thus spherical top molecules exhibit no rotation spectrum. Examples of spherical top molecules include  $\text{SF}_6$ ,  $\text{C}_{60}$ , and methane.



## Symmetric Tops

Symmetric top molecules have two equal moments of inertia and a third nonzero moment of inertia; that is,  $I_A \neq 0$  and  $(I_B = I_C) > I_A$ . Symmetric tops can either be prolate (long, like an egg) or oblate (flat, like a dish). Symmetric top molecules include  $\text{C}_6\text{H}_6$  (oblate),  $\text{NH}_3$  (prolate), and  $\text{CH}_3\text{Cl}$  (prolate). Because of the additional degree of freedom available, symmetric top molecules exhibit a more complicated energy structure, with energy levels given by

$$E_{J,k} = \frac{\hbar^2}{2} \left( \frac{J(J+1)}{I_B} + \left( \frac{1}{I_A} - \frac{1}{I_B} \right) k^2 \right) \quad (2.43)$$

where  $k$  is the component of the angular momentum about the axis which  $I_B$  is calculated from (called the *figure axis*) and thus may attain values determined by  $J$ .

$$k = J, J-1, J-2, \dots, -J \quad (2.44)$$

Thus for any  $J > 0$  the energy is doubly degenerate (since the energy depends on  $k^2$ ); there are  $2J+1$  combinations of  $J$  and  $k$  for a particular value of  $J$ . Again, a spectrum may only appear if the molecule in question has a permanent dipole moment; in such a case, selection rules dictate that transitions will occur between energy levels for which  $\Delta k = 0$  and  $\Delta J = 0, \pm 1$ .

## Asymmetric Tops

Asymmetric top molecules have three distinct moments of inertia ( $I_A \neq I_B \neq I_C$ ). Many of the molecules that exist within the temperature/pressure regimes of the

MHD generator concept (and the majority of molecules in general) are asymmetric tops, including  $\text{H}_2\text{O}$ ,  $\text{C}_2\text{H}_4$ , and  $\text{N}_2\text{O}_4$ . In this most general of cases, it is not possible to exactly express the energy levels of an asymmetric top molecule in the same way as for the molecules with higher symmetry.

In particular, there is no longer a preferred direction of rotation and the quantum number  $k$  used in Eq. 2.43 can no longer be given a physical meaning when the geometry of the molecule varies significantly from that of a symmetric top. Additionally, interaction effects which we ignored for the cases of symmetric and spherical tops are more problematic for asymmetric tops. There are  $2J + 1$  energy levels per value of  $J$  (still the total angular momentum quantum number); the degeneracy from the symmetric top case breaks (see Fig. 2.8). It is conventional to label each of these energy levels  $J_\tau$ , where  $\tau$  of course may take on the same values of  $k$  but does not carry the same interpretation as the angular momentum about the figure axis. Although we cannot exactly write  $J_\tau$ , we can determine it up to a numerical constant; where  $I_A \leq I_B \leq I_C$  we have

$$E_{J,\tau} = \frac{\hbar^2}{4} \left[ \left( \frac{1}{I_A} + \frac{1}{I_C} \right) J(J+1) + \left( \frac{1}{I_A} - \frac{1}{I_C} \right) E_\tau \right] \quad (2.45)$$

where  $E_\tau$ , called the reduced energy, has a numeric value determined by  $J$  and the asymmetry parameter  $\kappa$  is given by

$$\kappa = \frac{2I_B^{-1} - I_A^{-1} - I_C^{-1}}{I_A^{-1} - I_C^{-1}}. \quad (2.46)$$

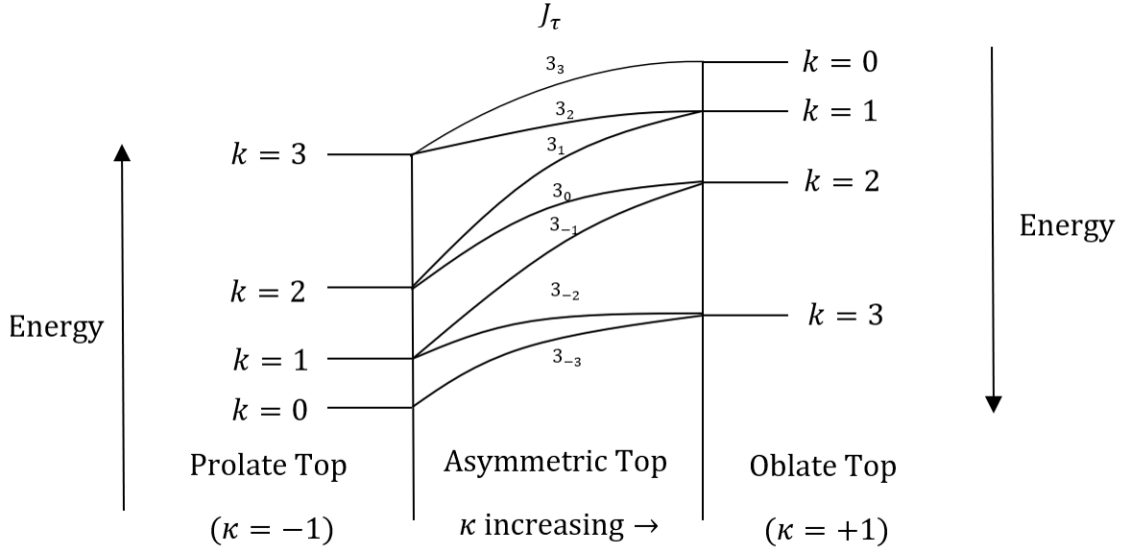


Figure 2.8: Qualitative schematic of the energy level splitting in asymmetric tops from symmetric tops for  $J = 3$ , slightly modified from a figure in [19], demonstrating the degeneracy-breaking of asymmetric tops.

It can be seen that  $\kappa$  ranges between  $-1$  and  $1$ . This parameter measures the prolateness (or oblateness) of the asymmetric top – for the special cases of a fully prolate or fully oblate symmetric top,  $\kappa$  takes on these exact values.  $E_\tau$ 's relationship with  $\kappa$  and  $J$  can be written implicitly for different values of  $J$ ; in particular, the relationship is polynomial [18]. Analytical solutions quickly become impossible as the degree of the polynomial increases above four. Numerical values of  $E_\tau$  are tabulated in other sources ([19]) for varying values of  $\kappa$  and  $J$ , allowing for accurate determination of rotational energy levels for a variety of molecules so long as the structure of the molecule is known. As usual, when observing an actual emission or absorption spectrum, rotational transitions are allowed only when the molecule has

a permanent dipole moment; and in such cases, transitions are allowed for  $\Delta J = 0$  or  $\Delta J = \pm 1$ .

### 2.5.2 Vibrational Spectra

While the theoretical determination of molecular rotation spectra is relatively straightforward, if not always exactly solvable, the determination of vibrational spectra is, at least superficially, considerably more problematic. The essential idea is much the same as for rotational spectra; each molecule has vibrational eigenfunctions which may absorb and emit energy much like electronic and rotational eigenfunctions. The contribution of molecular geometry to rotational modes is relatively simple; the spectrum is determined just by the three moments of inertia of the molecule. Vibrational modes, however, are considerably more complex because complicated molecular geometry necessitates detailed examination of normal modes of vibration. Depending on the shape of the molecule in question, a wide variety of normal modes are possible. As an approximation, it is useful to examine the classical theory of normal mode vibrations for molecules; it turns out to be highly relevant to the quantum mechanical treatment [18]. As with rotations, there is a rich phenomenology and vast amount of physics that go into describing vibrational spectra of polyatomic molecules; here we discuss the basic physics in order to understand the measurements that the NROS and FTIR systems will yield. Once again, we follow the exposition in [18].

## Mathematical Treatment

Given a molecule with  $N$  nuclei, we would in general need  $3N$  coordinates in order to describe the relative motion of the nuclei. If we are not interested in the overall translation of the molecule, then we may work in the center-of-mass rest frame and three degrees of freedom are removed; furthermore, not considering rotation about the center of mass removes an additional 3 coordinates. Thus, considering vibrations alone we have  $3N - 6$  degrees of freedom (although linear molecules, which require only two coordinates to specify the orientation of the molecule, will have  $3N - 5$  degrees of freedom); for most polyatomic molecules, this is considerably more than the 3 degrees of freedom for rotation. These degrees of freedom correspond to the  $3N - 6$  (or  $3N - 5$ ) normal modes of the molecule, each of which is associated with its own normal frequency; any complicated vibration can be decomposed into a superposition of these normal modes at different frequencies. Classical normal mode decomposition treats each of these normal modes as a simple harmonic oscillator, as if the atoms of the molecule were connected by Hookean springs. Although this model initially appears overly simplistic, it accurately calculates the same normal mode frequencies as the quantum mechanical treatment, to leading order.

The normal frequencies are most commonly determined using conservation of energy and the tools of classical dynamics. Because each particle  $i$  undergoes simple harmonic motion, we have

$$s_i = s_i^0 \cos(2\pi\nu t + \phi) \tag{2.47}$$

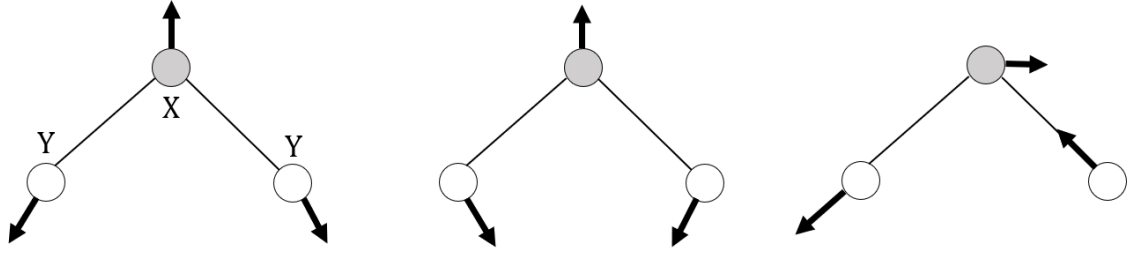


Figure 2.9: A triplet of normal mode vibrations for a bent  $XY_2$  model. Only the third triplet has a distinct energy – the other two are degenerate with each other.

where  $s_i$  is the displacement of particle  $i$  from equilibrium. Then the total energy is

$$H_i = V_i + T_i = \frac{1}{2}(4\pi^2\nu_i^2 m_i s_i^2 + m_i \dot{s}_i^2) \quad (2.48)$$

Let  $k_{q_1 q_2}^{ij}$  be the restoring force constant for particles  $i$  and  $j$  along dimensions  $q_1$  and  $q_2$ , then to first order near  $V = 0$  the potential energy is given by

$$V = \frac{1}{2} \sum_{ij} (k_{xx}^{ij} x_i x_j + k_{yy}^{ij} y_i y_j + k_{zz}^{ij} z_i z_j) + \sum_{ij} (k_{xy}^{ij} x_i y_j + k_{xz}^{ij} x_i z_j + k_{yz}^{ij} y_i z_j). \quad (2.49)$$

Then letting  $x_1, y_1, z_1, x_2, \dots = q_1, q_2, q_3, \dots$  we have

$$V = \frac{1}{2} \sum_{ij} k_{ij} q_{ij} \quad (2.50)$$

where  $k_{11} = k_{xx}^{11}$ ,  $k_{22} = k_{yy}^{11}$ ,  $\dots$ ,  $k_{12} = k_{xy}^{11}$  etc. The kinetic energy is

$$T = \frac{1}{2} \sum_{ij} b_{ij} \dot{q}_i \dot{q}_j \quad (2.51)$$

where  $b_{11} = b_{22} = b_{33} = m_1$ , and  $b_{44} = b_{55} = b_{66} = m_2$  etc and  $b_{ij} = 0$  for  $i \neq j$ . Then for appropriate choices of coefficients  $c_{ij}$  we can introduce a coordinate transformation

$$q_i = \sum_{j=1}^{3N} c_{ij} \eta_j \quad (2.52)$$

to the so-called “normal coordinates”  $\eta_j$  which will give us the energies of the system in a simpler form [20]:

$$V = \frac{1}{2}(\lambda_1 \eta_1^2 + \lambda_2 \eta_2^2 + \cdots + \lambda_{3N} \eta_{3N}^2)$$

$$T = \frac{1}{2}(\dot{\eta}_1^2 + \dot{\eta}_2^2 + \cdots + \dot{\eta}_{3N}^2)$$

where the  $\lambda_i$  are the  $3N$  roots of the characteristic equation

$$\begin{vmatrix} k_{11} - b_{11}\lambda & k_{12} - b_{12}\lambda & k_{13} - b_{13}\lambda & \cdots \\ k_{21} - b_{21}\lambda & k_{22} - b_{22}\lambda & k_{23} - b_{23}\lambda & \cdots \\ \vdots & \vdots & \vdots & \vdots \end{vmatrix} = 0 \quad (2.53)$$

where  $k_{ij}$  and  $b_{ij}$  are as defined above. Note here, however, that the form of the potential and kinetic energy reveals that the total energy  $H = T + V$  can be written as the sum of  $3N$  independent simple harmonic oscillators, each of which has a frequency implicitly given by  $\lambda_i = 4\pi^2\nu_i^2$ . Then we may obtain a version of the

characteristic equation in terms of our initial force constants and the masses;

$$\begin{vmatrix}
 k_{xx}^{11} - 4m_1\pi^2\nu^2 & k_{xy}^{11} & k_{xz}^{11} & k_{xx}^{12} & \cdots & k_{xz}^{1N} \\
 k_{yx}^{11} & k_{yy}^{11} - 4\pi^2m_1\nu^2 & k_{yz}^{11} & k_{yx}^{12} & \cdots & k_{yz}^{1N} \\
 k_{zx}^{11} & k_{zy}^{11} & k_{zz}^{11} - 4\pi^2m_1\nu^2 & k_{zx}^{12} & \cdots & k_{zz}^{1N} \\
 k_{xx}^{21} & k_{xy}^{21} & k_{xz}^{21} & k_{xx}^{22} - 4\pi^2m_2\nu^2 & \cdots & k_{xz}^{2N} \\
 \vdots & \vdots & \vdots & \vdots & \vdots & \vdots \\
 k_{zx}^{N1} & k_{zy}^{N1} & k_{zz}^{N1} & k_{zx}^{N2} & \cdots & k_{zz}^{NN} - 4\pi^2m_N\nu^2
 \end{vmatrix} = 0$$

which will yield the  $3N$  values for  $\nu_i$  that we require. The number of independent frequencies will be  $3N - 6$  (or  $3N - 5$ ) as mentioned before; the values of  $\nu_i$  obtained from the characteristic equation which correspond to these 6 (or 5) “missing” frequencies will be 0, and these values correspond to those “vibrations” which result in a net translation (3 of these) or rotation (3 of these for nonlinear molecules, or 2 for linear molecules) of the molecule. Of course, for the nontrivial values of  $\nu_i$  we may calculate the eigenvectors  $\mathbf{e}_i$  associated with these eigenvalues in the usual manner, and transforming back from the normal coordinates  $\eta_j$  to the original Cartesian set  $q_j$  will yield the precise form of the oscillations in the familiar coordinate system.

We turn now to the quantum formulation in order to calculate the energy levels. As in the rotational case, the energy levels of the vibrational system are determined by the solutions to Schrodinger’s equation for the molecule. The total Schrodinger equation for a system of  $N$  nuclei with coordinates  $x_i, y_i, z_i$  and masses  $m_i$  may be written [18]

$$\sum_{i=1}^N m_i \left( \frac{\partial^2 \psi}{\partial x_i^2} + \frac{\partial^2 \psi}{\partial y_i^2} + \frac{\partial^2 \psi}{\partial z_i^2} \right) + \frac{8\pi^2}{h^2} (E - V) \psi \quad (2.54)$$



where  $\psi$  is the wavefunction,  $E$  the total energy, and  $V$  the potential given in Eq. 2.49. Swapping to the normal coordinates  $\eta_i$  and applying separation of variables, the equation reduces to a sum of  $3N$  independent equations each of the form

$$\frac{1}{\psi_i} \frac{\partial^2 \psi_i}{\partial \eta_i^2} + \frac{8\pi^2}{h^2} (E_i - 2\pi^2 \nu_i^2 \eta_i^2) = 0$$

The astute reader may recognize this as Schrodinger's equation for  $3N$  individual harmonic oscillators. Then the total energy is  $E = \sum_i E_i$  where

$$E_i = h\nu_i \left( v_i + \frac{1}{2} \right), \quad v_i = 0, 1, 2, \dots$$

where  $v_i$  is the vibrational quantum number (note that this correctly gives the energy of the trivial solutions, with  $\nu_i = 0$ , as zero). Thus, the total energy may assume values of the form

$$E = h \sum_{i=1}^{3N} \nu_i \left( v_i + \frac{1}{2} \right)$$

for differing integer values of  $v_i$ , demonstrating the quantum nature of these vibrational energies.

As in the case with rotational spectra, the existence of quantized energy levels does not guarantee the existence of a spectrum with those energies. Emission of radiation is associated with a change in dipole moment, and as such only certain normal vibrations will result in radiation, as only certain configurations cause a change in dipole moment. Those which do are called *infrared active*, while those which do not are *inactive*. In the harmonic oscillator approximation only the fundamentals,

with frequencies  $\nu_i$ , are active (as opposed to the fundamentals and overtones). For molecules with no symmetry, all vibrational transitions are active; only those with sufficient symmetry are able to have inactive transitions. For example, in a linear  $XY_2$  molecule such as carbon dioxide, the symmetric stretching vibration does not cause a change in dipole moment and thus is inactive. That being said, vibrational emission/absorption lines are generally speaking far more abundant than rotational ones, since even molecules without a permanent dipole moment can exhibit them.

### 2.5.3 Roto-Vibrational Spectra

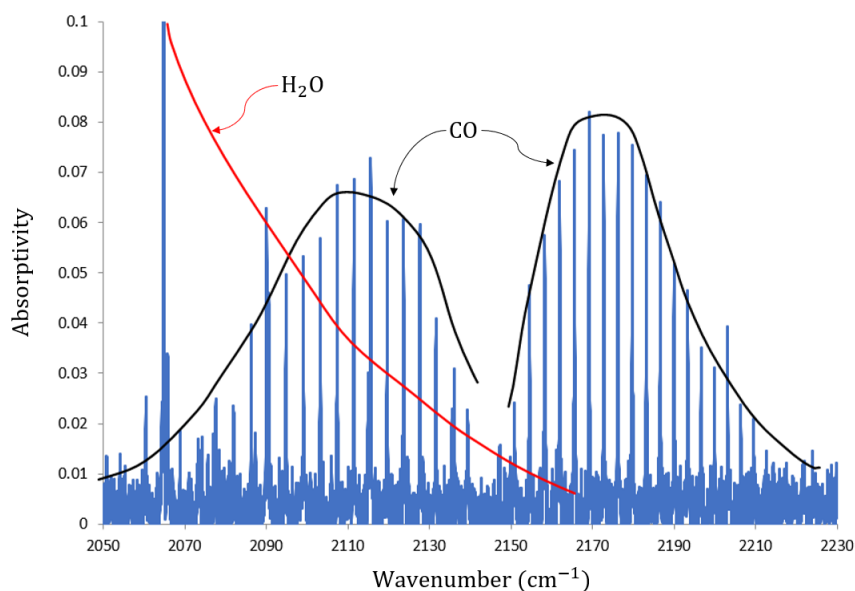


Figure 2.10: Roto-vibrational spectrum for carbon monoxide (CO), gathered by Jaworski et al with a newly-obtained FTIR spectrometer. Two bands in the CO spectrum are clearly visible (and approximately outlined in black), while an unrelated band from another species (likely water vapor) overlaps from the left and is outlined in red.

Putting together all of the molecular spectroscopy theory, we can construct a picture of what an actual molecular emission or absorption spectrum will look like; this involves taking into account both the rotational and vibrational transitions, and as a result is known as *roto-vibrational* spectroscopy. Rotational transitions are typically on a smaller energy scale than vibrational transitions; for a given vibrational state, many rotational lines will be evident. In the terminology of spectroscopy, rotational transitions form *lines* within the *bands* that are formed by vibrational transitions. The takeaway of this is that a molecular spectrum will typically resolve itself into larger-scale band structure within which will lie finer line structure, as seen in Fig. 2.10. This is relevant when one is considering which FTIR system will be suitable for their applications; although it does not require high spectral resolution to resolve the band structure, with separation on the order of  $50\text{ cm}^{-1}$  in wavenumber space, observing line structure is significantly more difficult, requiring resolution of around  $5\text{ cm}^{-1}$ .

Having concluded our theoretical discussion of the physics underlying both schlieren and infrared spectroscopic diagnostics, the next chapter will turn to an exploration of implementation concerns for the NROS diagnostic specifically, as it presents more unique difficulties than the FTIR system (which, as we mentioned, is relatively straightforward). Thus, the information that follows will be solely focused on schlieren systems.

# Chapter 3

## Implementation Concerns

### 3.1 Frequency Selection

This section explores some of the major considerations one must take into account when determining an appropriate frequency to probe using the NROS system, and thus the appropriate equipment (i.e. laser, detector) to use. This includes discussion of choosing an appropriate transition for the given species, and also how to determine the appropriate detuning away from resonance for the chosen transition.

#### 3.1.1 Determining an Appropriate Transition

The foremost consideration is what atomic transition to probe. Though this will primarily depend on the species one would like to examine, it is important to remember that not all species will have a transition that is easily tuned to. Furthermore, one must also consider the impact of the damping parameter and oscillator strength; a

particularly weak transition will have  $f_{0k}$  on the order of  $10^{-4}$  and will thus be unsuitable for obtaining a measurably high signal except at very high species densities.

For the purposes of the MHD generator experiment, the NROS system's goal is to measure the concentration of impurities in a plasma that result from contamination from its container. Because carbonate salt electrodes represent a possible improvement on current generator design, ions which readily form such salts are particularly important to consider. The table below shows some results for such ions that have transitions in the visible range (400-700 nm) that could be probed using the NROS system; note the wide range of values for oscillator strengths. Potentially important ones are marked with an asterisk (\*). All numerical values are taken from the NIST line database [14].

Atom	Transition	$\lambda$ (nm)	$f_{0k}$	$\gamma_k$
Li	$[\text{He}]2s, j = 1/2 \rightarrow [\text{He}]2p, j = 3/2$	670.776*	0.49797	$3.6891 \times 10^7$
	$[\text{He}]2s, j = 1/2 \rightarrow [\text{He}]2p, j = 1/2$	670.791*	0.24899	$3.6890 \times 10^7$
Na	$[\text{Ne}]3s, j = 1/2 \rightarrow [\text{Ne}]3p, j = 3/2$	588.9951	0.641	$6.16 \times 10^7$
	$[\text{Ne}]3s, j = 1/2 \rightarrow [\text{Ne}]3p, j = 1/2$	589.9524	0.320	$6.14 \times 10^7$
K	$[\text{Ar}]4s, j = 1/2 \rightarrow [\text{Ar}]5p, j = 3/2$	404.4136*	$5.69 \times 10^{-3}$	$1.16 \times 10^6$
	$[\text{Ar}]4s, j = 1/2 \rightarrow [\text{Ar}]5p, j = 1/2$	404.7208*	$2.63 \times 10^{-3}$	$1.07 \times 10^6$
	$[\text{Ar}]4s, j = 1/2 \rightarrow [\text{Ar}]4p, j = 3/2$	766.4899*	0.670	$3.80 \times 10^7$
	$[\text{Ar}]4s, j = 1/2 \rightarrow [\text{Ar}]4p, j = 1/2$	769.8965*	0.333	$3.75 \times 10^7$
Ca	$[\text{Ar}]4s^2, j = 0 \rightarrow [\text{Ar}]4s4p, j = 1$	422.673	1.75	$2.18 \times 10^8$

### 3.1.2 Frequency Detuning

Once an atomic transition to probe is chosen, a number of considerations go into the determination of an appropriate frequency to tune into in order to operate the schlieren system. Recalling our results from the previous chapter, we have that the index of refraction  $n$  in a dense medium as a function of frequency  $\omega$  and density  $\rho$  is given by

$$n(\rho, \omega) = 1 + \frac{\rho q_e^2}{2m_e \varepsilon_0} \sum_k \frac{(\omega_k^2 - \omega^2) f_{0k}}{(\omega_k^2 - \omega^2)^2 + \gamma_k^2 \omega^2} = 1 + \frac{\rho q_e^2 \xi(\omega)}{2m_e \varepsilon_0} \quad (3.1)$$

and the absorption coefficient by

$$a(\omega) = \frac{\rho q_e^2}{m_e \varepsilon_0 c} \sum_k \frac{\gamma_k \omega^2 f_{0k}}{(\omega_k^2 - \omega^2)^2 + \gamma_k^2 \omega^2} \quad (3.2)$$

where  $\omega_k$  are the frequencies of the resonances,  $f_{0k}$  are the oscillator strengths, and  $\gamma_k$  are the damping coefficients. Applying the Doppler broadening effect then yields the frequency-dependent quantities  $n_D$  and  $a_D$ . Additionally, recall that the response of the schlieren system depends strongly on the spatial dependence of the index of refraction. The near-resonance optical schlieren system links the frequency and density dependence of the index of refraction with the index of refraction dependence of the schlieren signal.

In short, for the NROS system we seek to maximize the density gradient of the index of refraction and thus to operate at frequencies near the resonant frequency of a transition  $\omega_0$ . A cursory glance at the form of  $n_D(\omega)$  will reveal that the value of  $\omega$  for which  $|n_D|$  (and thus  $\partial_\rho |n_D|$ ) is maximized is given by  $\omega_\mp = \sqrt{\omega_0^2 \pm \omega_0 \gamma}$ .

However, near these values the absorption coefficient  $a(\omega)$  is *also* very high and the plasma is nearly opaque. So, in practice it is preferable to choose a value of  $\omega$  that is near the peak in the index of refraction so that  $n(\omega)$  is still reasonably high, but far enough away that  $a(\omega)$  is acceptably low. The determination of this precise frequency depends on the spatial extent of the schlieren object<sup>1</sup>. A sufficiently thin schlieren object can suffer a higher value for the absorption coefficient than a thicker one, since proportionally more light will pass through simply as a result of the object's geometry. Thus, the determination of these values is quite sensitive to the specific implementation in question; we return to this question in our analysis of the sample coal arc later in this chapter.

## 3.2 Obtaining $\rho(r)$ from $\epsilon(y)$

As mentioned above, the simple one-dimensional schlieren system records intensity values in the image which correspond to the first derivative of the index of refraction. For our MHD column application the system geometry is more involved than for that of a one-dimensional schliere. As discussed in section 2.1, the MHD column is assumed to be an axisymmetric cylinder of plasma whose composition varies only as a function of radius. Thus, the schlieren object we are interested in will be effectively two-dimensional, with density gradient  $\rho(r)$  and thus index of refraction  $n(r)$ . Because the schlieren photograph records only the deflection angle as a function of the perpendicular distance from the optical ( $z$ ) axis, it is necessary to formulate a set of mathematical tools to obtain the radial profile we desire.

---

<sup>1</sup>Recalling that the absorption coefficient is defined so that the intensity  $I(z) = I_0 e^{-az}$

### 3.2.1 Abel Inversion

The first step is to obtain the index of refraction  $n(r)$  from the deflection  $\epsilon(y)$ . This is achieved through the use of an Abel inversion following the method in [21].

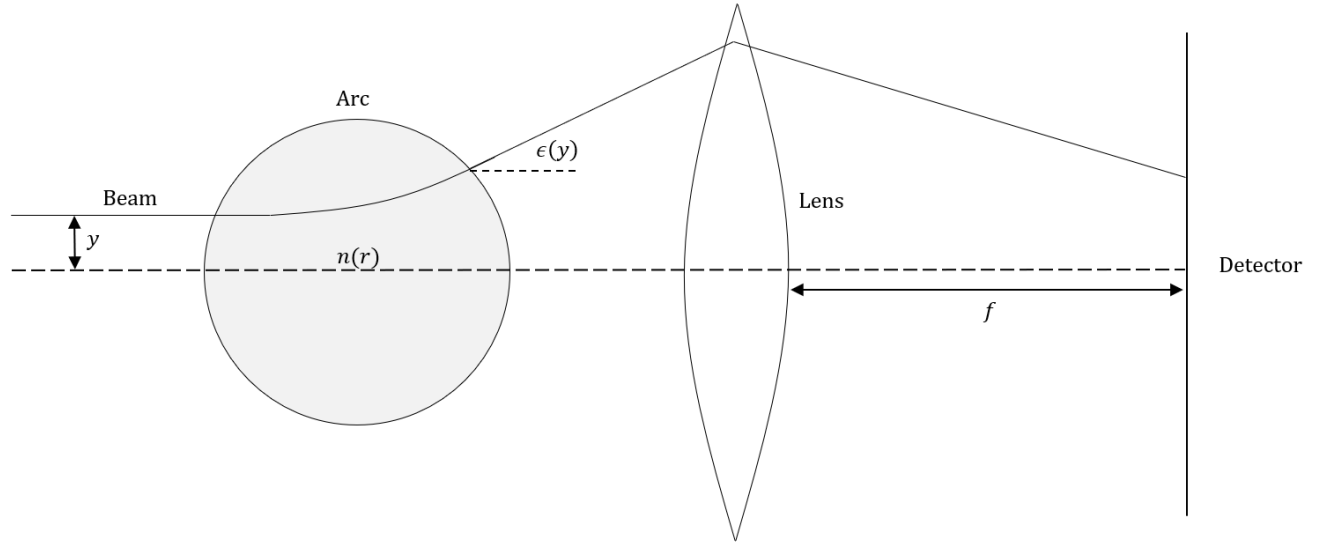


Figure 3.1: Cartoon of the arc system with optics in place, adapted from [21].

Supposing that the arc is axisymmetric, the path of the light beam  $\psi(r)$  will be given by the differential equation

$$\frac{d\psi}{dr} = \frac{yn_0}{r\sqrt{r^2n(r)^2 - y^2n_0^2}} \quad (3.3)$$

where  $n_0$  is the refractive index of the background medium (in this case air). The point at which the beam is closest to the center of the arc,  $r_0$ , is given implicitly by the equation  $r_0n(r_0) = yn_0$ . Then the total change in angle of the light beam along



the path pictured in the figure above will be given by

$$\Delta\psi = \int_{r_0}^{\infty} \frac{2yn_0}{r\sqrt{r^2n(r)^2 - y^2n_0^2}} dr \quad (3.4)$$

In the absence of the plasma column, the total angular change is just  $\pi$ , which means that the angular deflection  $\epsilon$  caused solely by the plasma column is given by

$$\epsilon(y) = \pi - \int_{r_0}^{\infty} \frac{2yn_0}{r\sqrt{r^2n(r)^2 - y^2n_0^2}} dr \quad (3.5)$$

To continue, we assume that  $rn(r)$  is monotonically increasing and that the plasma arc has  $n(r) = n_0$  for  $r > R$ . Then employ the change of variables  $s(r) = rn(r)/n_0$ ; taking the derivative with respect to  $s$ , we find

$$1 = \frac{1}{n_0} \left( r \frac{dn}{ds} + n \frac{dr}{ds} \right) \quad \rightarrow \quad \frac{1}{r} \frac{dr}{ds} = \frac{1}{s} - \frac{n'(r)}{n(r)} \frac{dr}{ds} \equiv \frac{1}{s} - f(s) \quad (3.6)$$

where the second term can be written  $f(s)$  since  $n(r)$  can be written as  $n(r(s))$ .

Applying this change of variables to the expression for  $\epsilon(y)$ , we obtain

$$\begin{aligned} \epsilon(y) &= \pi - 2y \int_y^{\infty} \frac{1}{s\sqrt{s^2 - y^2}} ds + 2y \int_y^R \frac{f(s)}{\sqrt{s^2 - y^2}} ds \\ &= 2y \int_y^R \frac{f(s)}{\sqrt{s^2 - y^2}} ds \end{aligned} \quad (3.7)$$

Using this expression for  $\epsilon(y)$ , we can show that

$$\int_s^R f(t) dt = -\log \left( \frac{n(r)}{n_0} \right) = \frac{1}{\pi} \int_s^R \frac{\epsilon(y)}{\sqrt{y^2 - s^2}} dy \quad (3.8)$$

and therefore that the solution we desire is given by

$$n(s) = n_0 \exp \left( -\frac{1}{\pi} \int_s^R \frac{\epsilon(y)}{\sqrt{y^2 - s^2}} \right) \equiv n_0 e^{-\phi(s)} \quad (3.9)$$

where

$$r(s) = \frac{sn_0}{n(s)} = s e^{\phi(s)} \quad (3.10)$$

and we have arrived at an expression that gives the index of refraction  $n(r)$  as a function of the angular deflection  $\epsilon(y)$  (which, of course, is recorded in the contrast data in the final image).

### 3.3 Determining $\rho(r)$ from $n(r)$

In principle, the determination of  $\rho(r)$  from  $n(r)$  is quite straightforward. Recall that the previous chapter yielded a result for the index of refraction  $n$  in a dense medium as a function of frequency  $\omega$  and density  $\rho$  as

$$n(\rho, \omega) = 1 + \frac{\rho q_e^2}{2m_e \epsilon_0} \sum_k \frac{(\omega_k^2 - \omega^2) f_{0k}}{(\omega_k^2 - \omega^2)^2 + \gamma_k^2 \omega^2} = 1 + \frac{\rho e^2 \xi(\omega)}{2m_e \epsilon_0} \quad (3.11)$$

and the absorption coefficient

$$a(\omega) = \frac{\rho q_e^2}{m_e \epsilon_0 c} \sum_k \frac{\gamma_k \omega^2 f_{0k}}{(\omega_k^2 - \omega^2)^2 + \gamma_k^2 \omega^2} \quad (3.12)$$

where  $\omega_k$  are the frequencies of the resonances,  $f_{0k}$  are the oscillator strengths, and  $\gamma_k$  are the damping coefficients. Each of these values may be found tabulated for

a variety of species [14], and thus in principle it is straightforward to analytically calculate  $\xi(\omega)$  (as well as the corresponding frequency-dependent part of  $a$ ). From this result, we apply the Doppler broadening correction at the relevant temperature (using either the delta function approximations mentioned in that section, or for more detailed calculations running a full convolution with the Gaussian) and simply read off the density.

### 3.4 Instrumentation Considerations

Naturally, instrumentation will vary widely depending on the species present in the plasma arc in question. The center frequencies at resonance place the strictest requirements on the kind of lasers (and detectors) that may be used, as these transitions may have any frequency from ultraviolet to infrared (or even outside this range, though this is rarer). Tunable lasers in these frequency ranges are widely available, and many have the picometer tuning necessary to operate at the requisite part of the refractivity and absorption curves; which laser to choose will simply be a matter of what species is being probed.

The optical components which make up the rest of the schlieren system, such as mirrors and lenses, are less problematic and not, in general, specialized for a specific species. High-quality mirrors and lenses for visible and near-visible light as well as apertures and slits can be obtained at reasonable cost from many optical instrument providers, though it is worth noting that should one be interested in lower wavelength transitions (for example, the  $n = 1$  transitions in hydrogen) that more precisely

constructed and polished mirrors may be necessary. For reference, we list some possible optical components that have proven to be effective in two-color schlieren applications that would certainly be adaptable to the proposed visible-regime tunable schlieren diagnostic in Appendix A. As for actual construction, there is a priori no reason to stray from the traditional Z-type schlieren system, although space concerns and the physical size of the tunable laser may necessitate slight modification.

### 3.5 Sample Coal Arc

In this section we analyze the equation for  $n(\omega)$  and use a simulated plasma arc to obtain an idea of the kind of profiles we might examine using the NROS system.

Fuels	
Species	Weight Fraction
C (graphite)	0.9099
H <sub>2</sub>	0.06345
K <sub>2</sub> CO <sub>3</sub>	0.02665
Oxidizer	
Species	Weight
O <sub>2</sub>	2312 g

As mentioned above, we would like to have our resonance of interest be in the visible range; a convenient transition exists in potassium, with a wavelength of 404.72 nm [14]. One MHD generator concept involves the use of liquid salt electrodes; in particular, Jaworski et al. are interested in the possibility of potassium carbonate

( $K_2CO_3$ ) electrodes. Plasma-wall interactions introduce the possibility of potassium in the arc stream, and thus a predictive model for measuring the concentration of potassium in the arc is desirable. The plasma arc composition code discussed section 2.1 was used to predict the radial composition of a simulated coal-burning plasma arc, with initial composition tabulated below. From the arc simulation code, we are able to obtain a radial map of of temperature (Fig. 3.2) as well as relative concentration of potassium (Fig. 3.3).

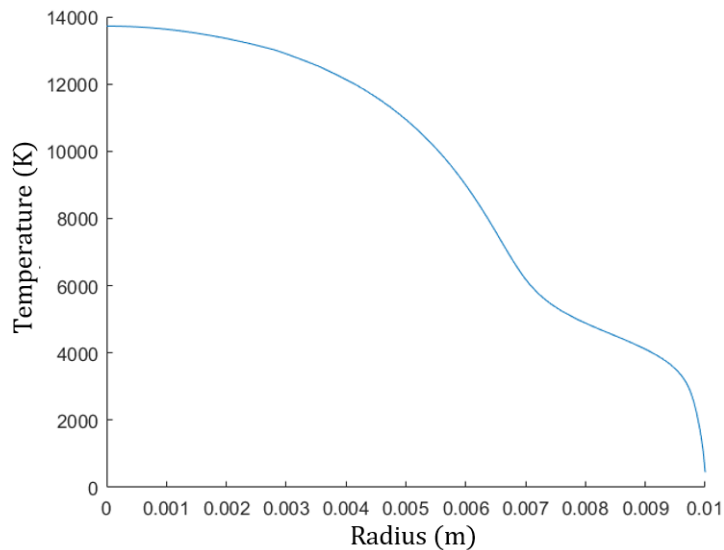


Figure 3.2: Temperature map in the sample arc.

We then generate a Doppler broadening profile (one-dimensional Maxwellian) for each temperature in the radial temperature map, then calculate the naturally broadened index of refraction and absorption coefficient for each density and temperature in the species map. Finally, at each radial point we perform the convolution with the corresponding Doppler broadening profile in order to obtain radial maps of the index

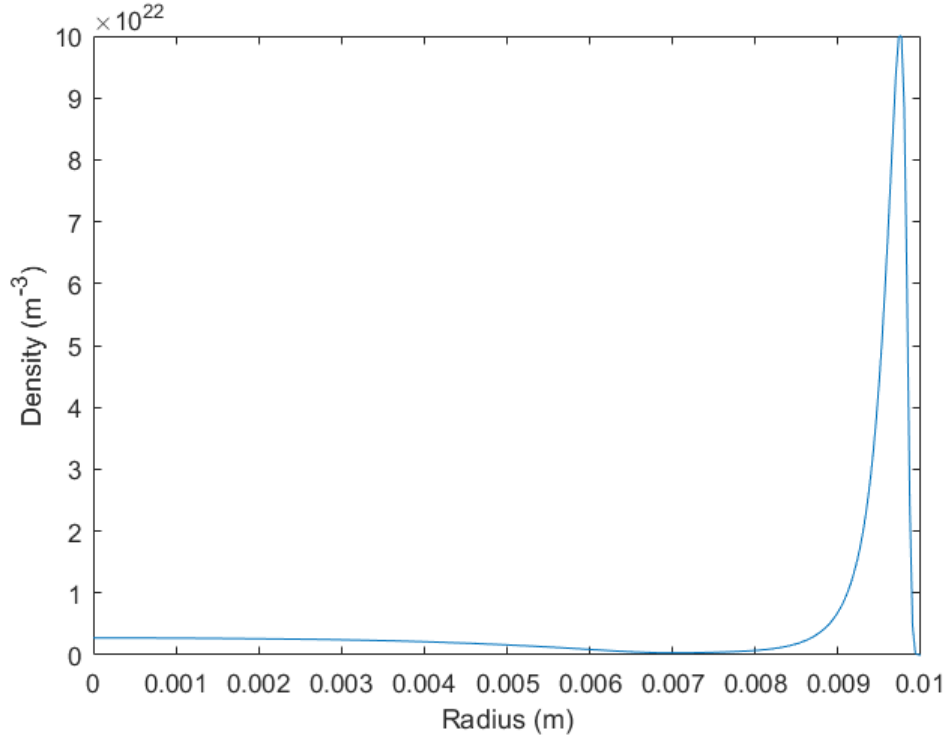


Figure 3.3: Map of (neutral) potassium in the arc.

of refraction and absorption coefficient at each wavelength. For reference, recall that potassium has two transitions in the visible range, one at 404.4136 nm and one at 404.7207 nm. Although these seem very “close”, the peaks are actually quite far apart relative to their widths. Nonetheless, we use both in our calculations of the absorption coefficient and refractive index; the figures, however, show only the region near the  $\lambda = 404.7207$  nm peak. Absorption profiles are given below.

One might naively expect the absorption and index of refraction profiles to have roughly the same shape for all frequencies, just scaled appropriately for the gradients in the density of potassium. This is *not* the case, due to the variations in profile

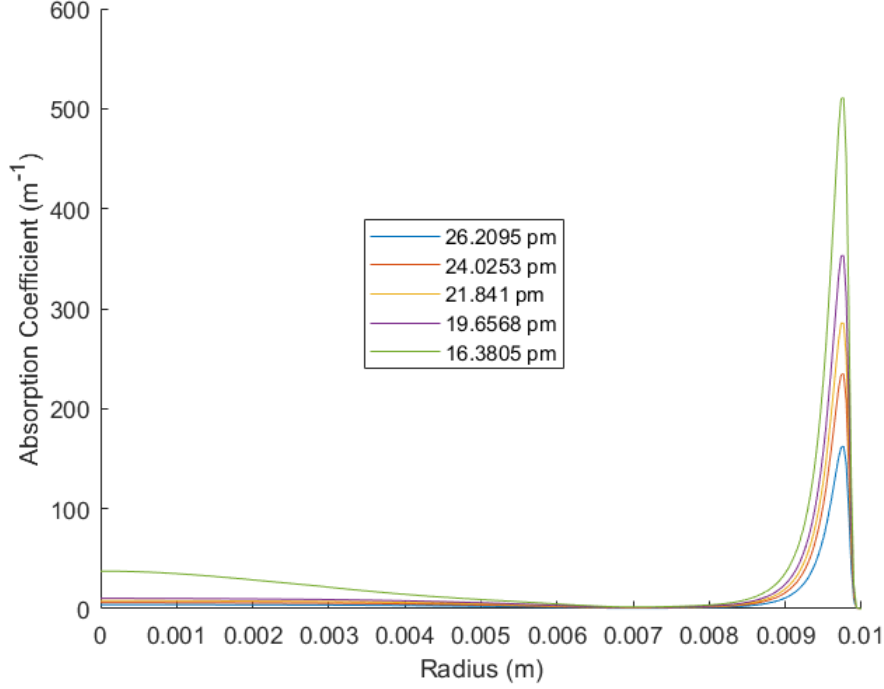


Figure 3.4: Absorption coefficient for wavelengths farther away from resonance. Legend denotes magnitude of detuning from resonant wavelength.

shape that result from temperature gradients that affect the Doppler broadening mechanism. Far from resonance, the shapes match naive expectations, as shown in Fig. 3.4. Closer to resonance they are dramatically different for absorption, as shown in Fig. 3.5. This is because the high temperature at the arc's center results in a very broad resonance peak that picks up frequencies more readily; far from resonance, however, the frequencies remain outside the range of the peak. The takeaway from this plot is that one really cannot afford to operate too close to resonance; for a reasonable 1 cm optical depth, if we operate at 5 pm detuning almost identically zero transmission will occur (intensity will decrease on the order of  $10^{-4000}$ ).

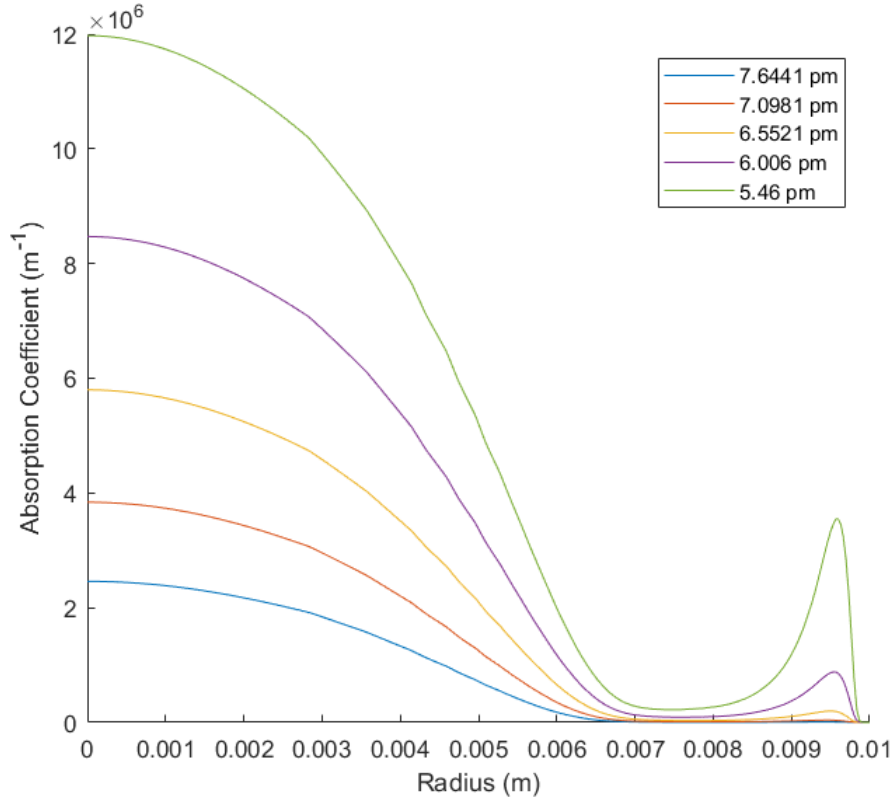


Figure 3.5: Absorption coefficient for wavelengths quite close to the resonance. Note the fantastic sensitivity to wavelength in this regime, where changing the detuning by only 2  $\mu\text{m}$  increases the absorption by a factor of six.

Changes in the index of refraction are more modest, because Doppler broadening does not affect the shape of refractivity curves as strongly. The actual value for refractivity, shown below in Fig. 3.6, still changes quite noticeably.

Again, we reiterate that an appropriate detuning amount likely depends on the actual geometry of the system. For this particular arc, a happy medium between enhanced index of refraction and modestly low absorption coefficients seems to be at about  $\lambda = 404.74 \text{ nm}$ , which corresponds to a detuning on the order of 10  $\mu\text{m}$ . This



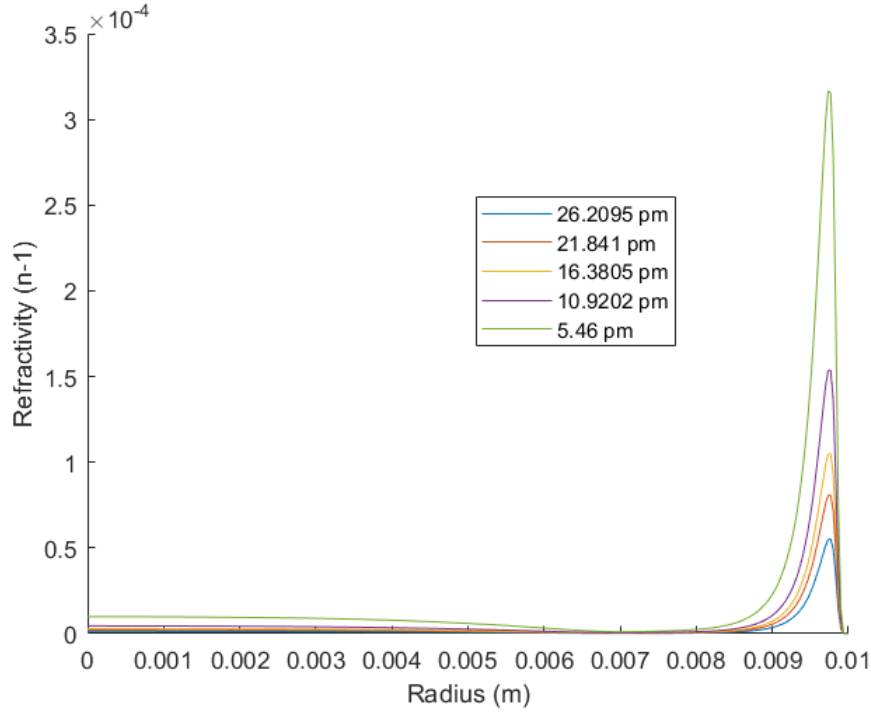


Figure 3.6: Refractivity ( $n - 1$ ) map for frequencies near resonance. Again, legend denotes magnitude of detuning from resonance.

wavelength has an index of refraction response about three times higher than that far from resonance, and has an absorption coefficient about  $10^4$  times lower than that closer to resonance.

### 3.5.1 Quantitative Wavelength Selection

Looking at the curves provides us with a decent estimate of what wavelength we should use to probe the plasma. However, a quantitative analysis is preferable to have greater assurance that the value we find is in fact the ideal one. We begin by

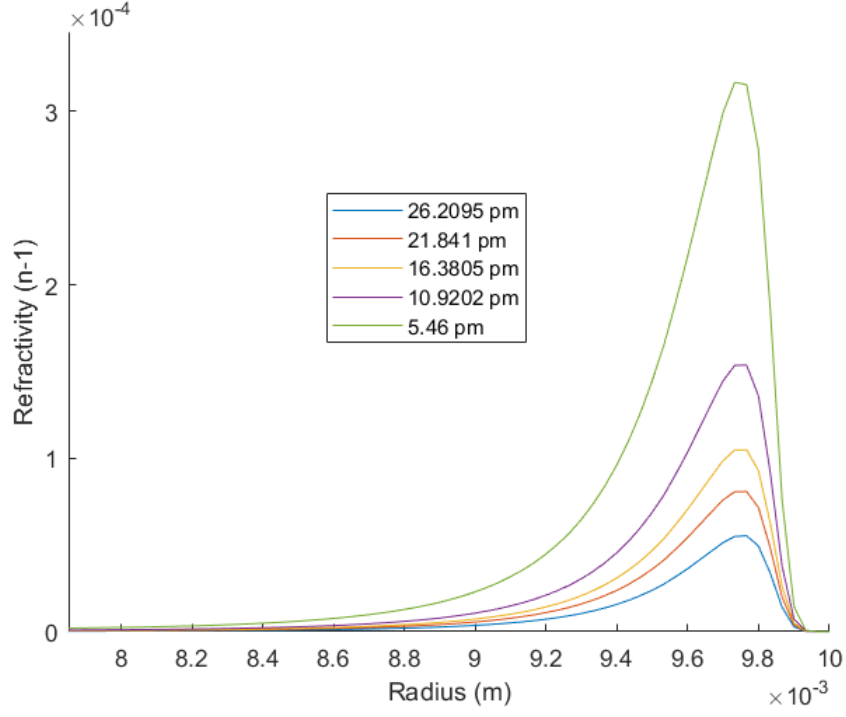


Figure 3.7: Enlarged version of Fig. 3.6 to show the detail near the outer arc region, where potassium density is highest.

recalling from Eq. 2.17 that the contrast in a schlieren image is given by

$$C = \frac{f_2}{a} \epsilon(y)$$

where  $f_2$  is the focal length of the second mirror,  $a$  is the schlieren cutoff, and  $\epsilon(y)$  is the deflection as a function of  $y$ . At the ideal wavelength, we want this quantity to be maximized, and thus we seek to find the value of  $\lambda$  for which  $\epsilon(y)$  is maximized. However, we should note that if absorption is too high, then we can get no useful data at all. Additionally, we should also associate some kind of loss term with finite

absorption, since low photon throughput can make it difficult to discern differences in contrast in the final schlieren image. With these considerations in mind, we set out to develop a “utility function”  $U(y, \lambda)$  that we can maximize to find the ideal wavelength<sup>2</sup>.

First we should consider the deflection  $\epsilon(y)$ . We have from Eq. 3.5 that the deflection is given by

$$\epsilon(y, \lambda) = \pi - \int_{r_0}^R \frac{2yn_0}{r\sqrt{r^2n(r, \lambda)^2 - y^2n_0^2}}dr = \pi - \int_{r_0}^R \frac{2y}{r\sqrt{r^2n(r, \lambda)^2 - y^2}}dr \quad (3.13)$$

where  $r_0n(r_0, \lambda) = y$ ,  $R$  is the radius of the plasma column, and  $n_0$  is the index of refraction outside the plasma column (which we will take to be unity). In this case, we have numerical values for  $n(r, \lambda)$  at each wavelength  $\lambda$  we are interested in, and for simplicity’s sake we will consider fixing  $y$  at some intermediate value, say  $y = 0.5$  cm. For each wavelength, we need to numerically calculate  $r_0$  (since the exact functional form of  $n(r)$  is unknown), but once that is done it is relatively easy to calculate  $\epsilon$  by making use of Matlab’s `cumtrapz` function for approximating integrals.

Next considering absorption, we can quantify the amount of light absorbed as the beam traverses the arc by defining the absorption factor  $q(y, \lambda)$ :

$$q(y, \lambda) \equiv \int_{\psi(y)} a(r, \lambda)dr \quad (3.14)$$

---

<sup>2</sup>It is worth noting that because the both refractivity and absorption are symmetric about the resonance, detuning on either side will provide the same quality of sensitivity. We arbitrarily use “ideal wavelength” to refer to the one which has a lower frequency.

where the integral is taken along the optical path  $\psi$ . Selecting a point at which the absorption is “too much” is somewhat arbitrary by nature; we can suppose that too much light is lost if the ratio falls to some cutoff value  $I/I_0 = r$ , then the absorption factor  $q_c = -\log(r)$  represents the highest absorption factor we are willing to endure. This suggests that the entire utility function should have a prefactor of something like  $-H(q(y, \lambda) - q_c) + 1$ , where  $H(x)$  is the Heaviside step function. This prefactor will take on a value of unity where  $q(y, \lambda) < q_c$  and is zero where  $q(y, \lambda) \geq q_c$ , corresponding to no utility (no useful data) when absorption is too high. Finally, some kind of loss term should be associated with absorption even for wavelengths lower than the critical value. We suggest weighting the absorption factor  $q(y, \lambda)$  with some constant factor  $\zeta$  that can be adjusted depending on how sensitive the implementation in question is to photon throughput. Putting it all together, we propose a utility function  $U(y, \lambda)$  as follows;

$$U(y, \lambda) = \left(1 - H(q(y, \lambda) - q_c)\right) (\epsilon(y, \lambda) - \zeta q(y, \lambda)) \quad (3.15)$$

As with most utility functions, the actual value of this function doesn’t really carry any specific meaning; however, the point for which the function is maximized represents the ideal wavelength subject to our constraints and the weighting factor  $\zeta$ .

Because it is not straightforward to calculate the deflection path  $\psi(y)$ , it is worth considering approximation methods for the absorption factor  $q(y, \lambda)$  that do not involve integrating along  $\psi$ . For a pessimistic estimate, we can assume that the optical length is the longest possible 2 cm (for our arc) and that incoming light experiences the maximum value of absorption at the given wavelength over the entire

spatial extent of the arc; that is, we may write

$$q(\lambda) = 0.02 \max(a(r, \lambda)) \quad (3.16)$$

This quantity is guaranteed to overestimate  $q(\lambda)$ , but it is easy to compute and will give a realistic estimate for the absorption factor. With that in mind, we may calculate values for the utility function at each wavelength  $\lambda$  for a given  $y$  and find the maximum in order to determine the ideal wavelength.

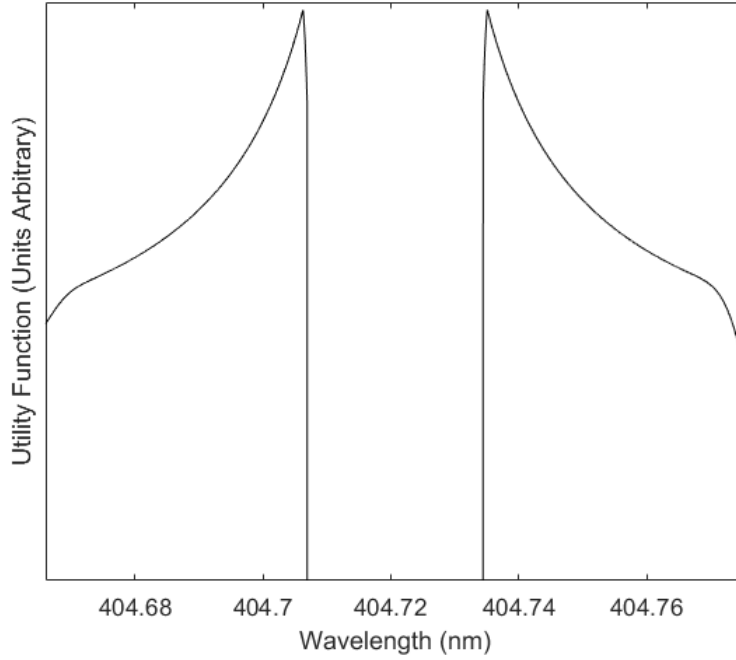


Figure 3.8: The utility function for the coal arc at  $y = 0.5$  cm, with  $\zeta = 0.1$  and  $q_c = 4.6$ . The ideal wavelengths are clearly identifiable.

For this particular coal arc, as wavelengths approach resonance the absorption increases much faster than the refractivity, resulting in a utility function with very

sharp peaks, as seen in Fig. 3.8. Depending on our value of  $\zeta$ , we obtain different ideal wavelengths and in general smaller values of  $\zeta$  will give correspondingly smaller ideal detunings until the absorption factor passes the cutoff value. For an absorption cutoff limit at  $q_c = 4.6$  (corresponding to about 1% transmittance), and for light incoming at  $y = 0.5$  cm, using a weighting of  $\zeta = 0.1$  yields an ideal wavelength of 404.7351 nm (detuning of 14.4 pm). This is close to our naive prediction from gross analysis of the plots. For certain applications, it also seems reasonable to assign  $\zeta = 0$ , in the sense that if a meaningful measurement can be made, slightly more absorption can be considered acceptable. For  $\zeta = 0$  we get an ideal wavelength of 404.7344 nm (detuning of 13.7 pm).

### 3.6 FTIR and NROS, Together

Both the FTIR and NROS systems supply methods for determining the composition of a plasma arc, so one might wonder if there is any new information to be gained by using the two simultaneously. Indeed, the fact that they can provide the same information is precisely why the two diagnostics are so valuable together. In essence, the two diagnostics can be used to calibrate each other on species that each can examine, allowing absolute measurements to be taken on each that the other could not achieve. For example, the two diagnostics could each be used to measure the concentration map of potassium or lithium, each of which have transitions suitable for NROS in the near-infrared, and are probeable by the FTIR system due to their low transition frequencies. Once the two devices are properly calibrated

against each other, the FTIR system is able to determine concentration maps for polyatomic molecules that are generally more difficult to measure using the NROS system, due to their relatively weak electronic transitions. Meanwhile, the NROS system could probe atomic species with electronic transition frequencies that are not in the infrared, which would be inaccessible to the FTIR system due to their lack of rotational and vibrational transitions. In this way, the two devices used together can obtain a more complete reconstruction of arc composition than either alone could achieve. This is in some ways the Holy Grail of nonintrusive plasma diagnostics.

# Chapter 4

## Conclusion

When designing a plasma experiment, a variety of factors must be considered in order to determine the optimal diagnostic arrays to use in order to obtain the most useful, complete data possible. In this thesis, we have introduced the theory behind two promising but little-explored diagnostics in the field of plasma physics, outlined their advantages and limitations, and developed robust modeling tools to aid in the implementation of one of them. Because of time limitations, experimental work and physical construction have proven to be beyond the scope of this thesis; thus, in this chapter, we reiterate what we perceive to be the most important points of the preceding discussion and also expand on some of the steps that could be taken moving forward with the MHD generator experiment.

In terms of physical theory, the most critical point to keep in mind is the effect of Doppler broadening on the absorption and index of refraction profiles in a plasma arc. In low-temperature applications this effect may be negligible, but in



plasma applications where ion temperatures may be on the order of 1 eV, Doppler broadening is extremely influential in determining the actual shape of the absorption and refraction profiles, and in order to obtain an accurate estimate for composition profiles a good model for arc temperature will be necessary. That being said, for applications with plasmas that are not fully ionized like the ones explored in this thesis, the combination of natural and Doppler broadening suggests that optimal detuning from resonance for an NROS diagnostic system will generally be on the order of 10 picometers: any closer to resonance and the absorption will be far too high; and any farther away the index of refraction response will be too low to accurately measure.

We feel that this thesis represents a significant step forward in the development of optical diagnostics. The capability of simulating the conditions in a plasma arc to the extent that we are able to construct radial index of refraction curves is quite valuable, and to the best of our knowledge a quantitative method for discerning an ideal probing wavelength is unique.

## 4.1 Future Directions

The natural next step in this project would be to construct the physical NROS and FTIR diagnostic systems. For the MHD project specifically, an FTIR system has been procured and implementation of the system's optics will likely begin soon, to coincide with the construction of the experimental arc system. As for the NROS system, further consideration must be done to decide what sort of tunable laser (and, correspondingly, what sort of detector) should be procured. With the goal of

utilizing the complementary aspects of the two systems and most likely measuring lines from potassium in mind, a laser which can scan over the near infrared as well as some of the visible spectrum is probably desirable. Ultimately, we hope to implement NROS and FTIR to better the energy production of the world at large.

# Bibliography

- [1] United States Energy Information Administration. Monthly energy review (december 2017). 2017.
- [2] Richard J. Rosa. *Magnetohydrodynamic Energy Conversion*. Hemisphere Pub. Corp, 1987.
- [3] United States General Accounting Office. Report to chairman, subcommittee on energy, committee on science, space, and technology, house of representatives: The department of energy’s magnetohydrodynamics development program, 1993.
- [4] Richard Dendy. *Plasma Physics: An Introductory Course*. Cambridge University Press, 1996.
- [5] S. Gordon and B. J. McBride. Computer program for calculation of complex chemical equilibrium compositions and applications. *NASA Reference Publication 1311*, 1996.
- [6] P. Gueye, Y. Cressault, V. Rohani, and L. Fulcheri. A simplified model for the determination of current-voltage characteristics of a high pressure hydrogen plasma arc. *Journal of Applied Physics*, 121:073302, 2017.
- [7] Y. Itikawa et al. Cross sections for collisions of electrons and photons with oxygen molecules. *Journal of Physical Chemistry, Reference Data*, 18(1):23.
- [8] Yukikazu Itikawa. Cross Sections for Electron Collisions With Carbon Dioxide. *Journal of Physical and Chemical Reference Data*, 31(3):749–767, September 2002.
- [9] James E. Land. Electron scattering cross sections for momentum transfer and inelastic excitation in carbon monoxide. *Journal of Applied Physics*, 49(12):5716–5721, December 1978.

- [10] Yukikazu Itikawa and Nigel Mason. Cross Sections for Electron Collisions with Water Molecules. *Journal of Physical and Chemical Reference Data*, 34(1):1–22, March 2005.
- [11] S. J. et al Buckman. *Interactions of Photons and Electrons with Atoms*. Springer, 2000.
- [12] G. S. Settles. *Schlieren and Shadowgraph Techniques: Visualizing Phenomenon in Transparent Media*. Springer, 2001.
- [13] Daniel A. Steck. *Quantum and Atom Optics*. available online at <http://steck.us/teaching> (revision 0.12.0.), 2017.
- [14] A. Kramida, Yu Ralchenko, J. Reader, and NIST Team. Nist atomic spectra database (ver. 5.5.3). National Institute of Standards and Technology (available <https://physics.nist.gov/asd>), 2018.
- [15] Maxwell speed distribution directly from boltzmann distribution. <http://hyperphysics.phy-astr.gsu.edu/hbase/Kinetic/maxspe.html>. Accessed: 2018-03-25.
- [16] Ian Howarth. Phas 2112: Astrophysical processes from nebulae to stars lecture notes. <http://zuserver2.star.ucl.ac.uk/~idh/PHAS2112/>. Lecture 8: Accessed: 2018-03-25.
- [17] Peter R. Griffiths and James A. De Haseth. *Fourier Transform Infrared Spectroscopy*. John Wiley and Sons, Inc., 2007.
- [18] G. Herzberg. *Infrared and Raman Spectroscopy*. Lancaster Press, Inc., 1956.
- [19] J. W. Blaker, M. Sidran, and A. Kaercher. Rotational energy levels of asymmetric top molecules. *Grumman Aircraft Engineering Corp., Research Department*, 1962.
- [20] S. Thornton and J. Marion. *Classical Dynamics of Particles and Systems*. Thomson Learning, Inc., 2 edition, 2004.
- [21] U. Kogelschatz and W. R. Schneider. Quantitative schlieren techniques applied to high current arc investigations. *Applied Optics*, 11, 1972.

# Appendix A

## Possible Instrumentation

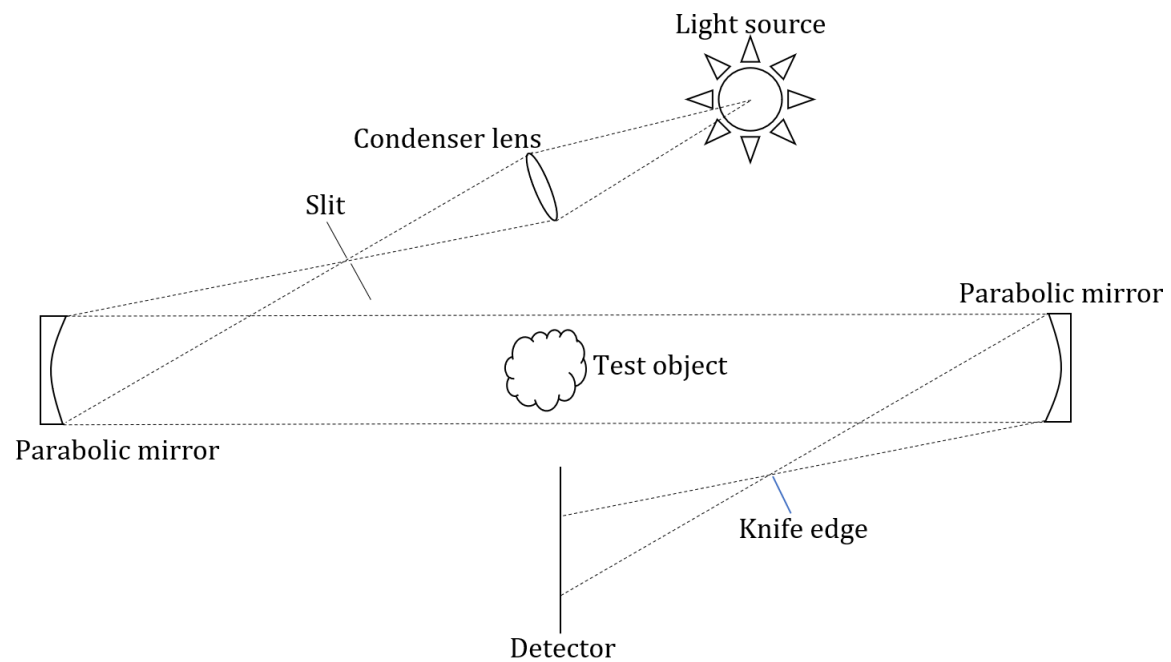


Figure A.1: Z-type schlieren diagram, for reference

1. Thorlabs LA1255 plano-convex lens (condenser lens)

2. Thorlabs CP20S circular iris
3. Thorlabs VA100C slit system
4. 2x Edmunds PF20-03-F01 planar mirrors (for redirecting light because of table geometry restrictions)
5. 2x Edmund's 4.25" diameter 25.5" focal length parabolic mirrors
6. 2x custom Thorlabs CXY2 knife-edge mountings (one for each spatial direction)
7. 2x Thorlabs LA1257-A converging lenses (for focusing)
8. 2x Thorlabs LB1471-A biconvex lenses
9. 2x Thorlabs LD1464-A biconcave lenses
10. CVI laser optics PLCX-25.4-1545.0-C lens (for calibration measurements)

Naturally, one must additionally acquire mountings and posts to accommodate each of these components properly; such equipment is readily available from Thorlabs.

Optics aside, the other major consideration is a light source which is tunable over the frequency range desired. Tunable lasers are available on the market for a variety of different wavelength regimes from high-energy visible down to the infrared; choosing which to use is simply a matter of what species one wishes to probe.

# Appendix B

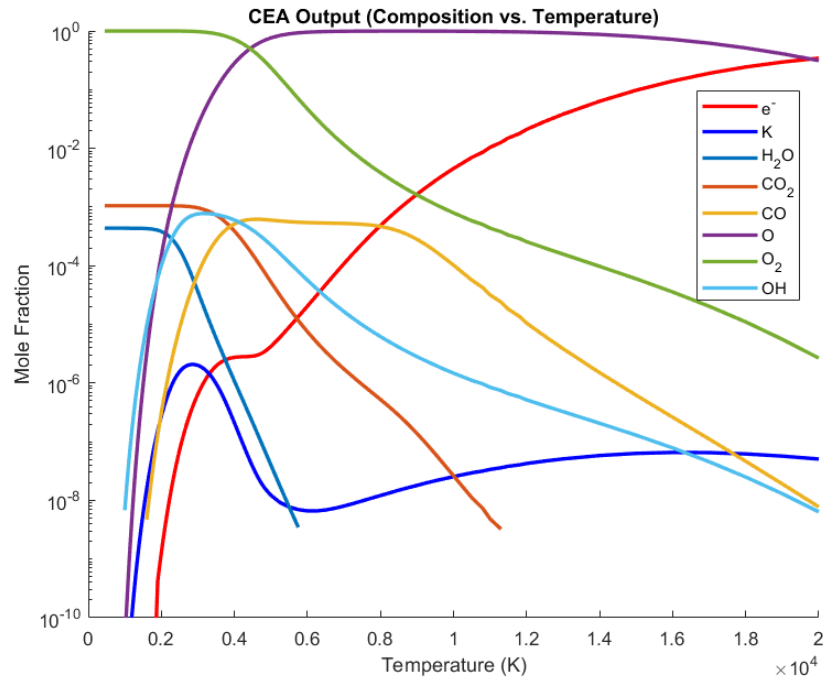
## Sample Arc Code Results

Here we include some of the output from the arc code for the plasma arc that we examined in chapter 3.

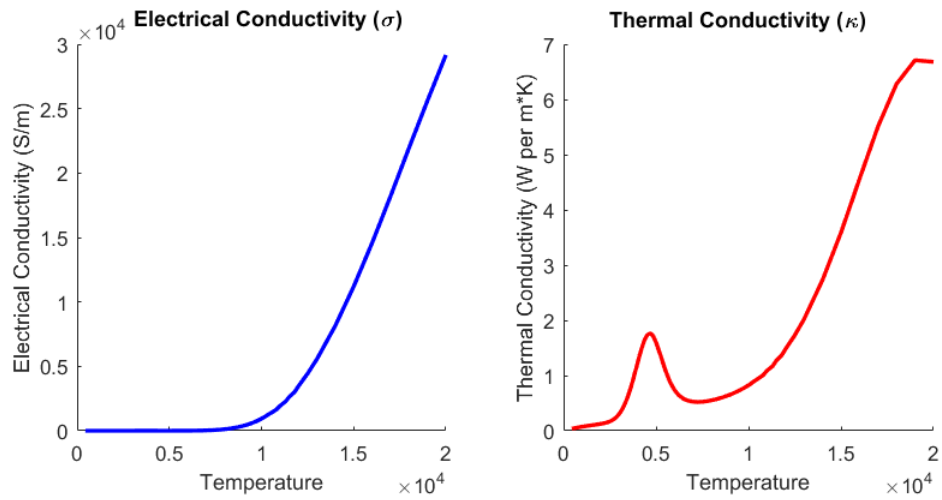
As we mentioned, first data is taken from CEA for use in calculations by the arc code. Shown below is a sample of such data for a simple hydrogen arc (used because of space concerns).

t	rho	cond	e-	H	H2	m
4.5E+02	2.1837E-02	1.6882E+01	0.00E+00	0.0E+00	1.00E+00	2.0159E+00
5.0E+02	1.9653E-02	1.7808E+01	0.00E+00	0.0E+00	1.00E+00	2.0159E+00
6.0E+02	1.6378E-02	1.9547E+01	0.00E+00	0.0E+00	1.00E+00	2.0159E+00
.	.	.	.	.	.	.
.	.	.	.	.	.	.

From this data, the script constructs models for the plasma's composition (in mole fractions) as a function of temperature, as shown in the following figure.

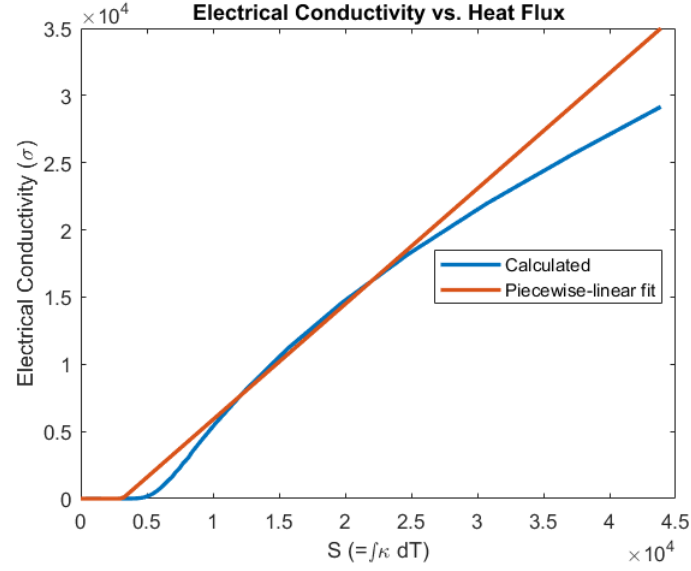


Next the code calculates thermal and electrical conductivity as functions of temperature from the composition.

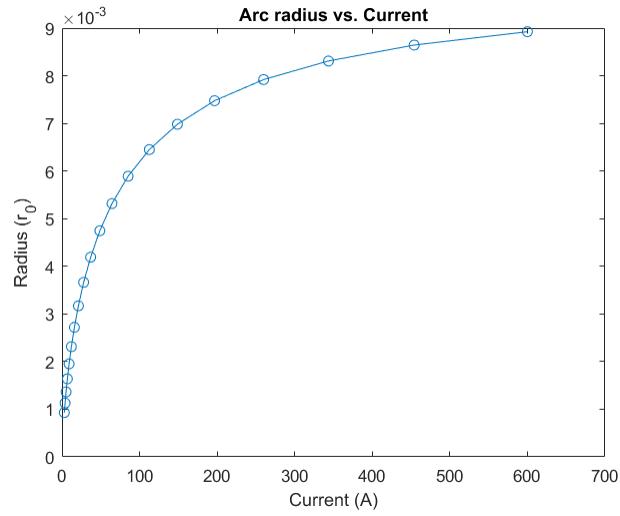




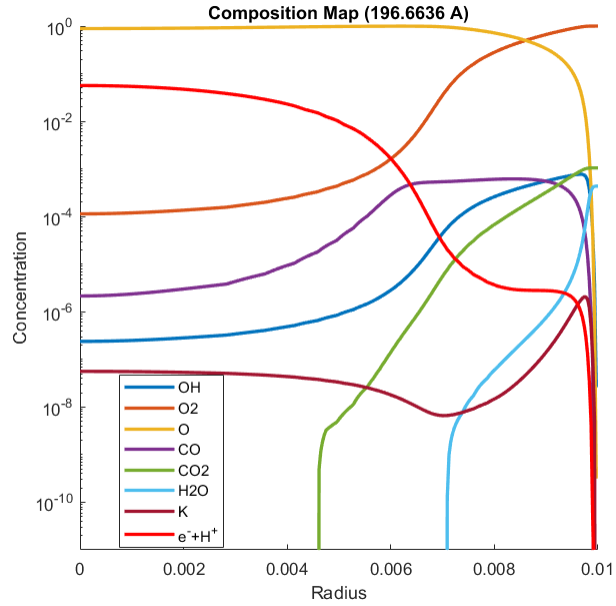
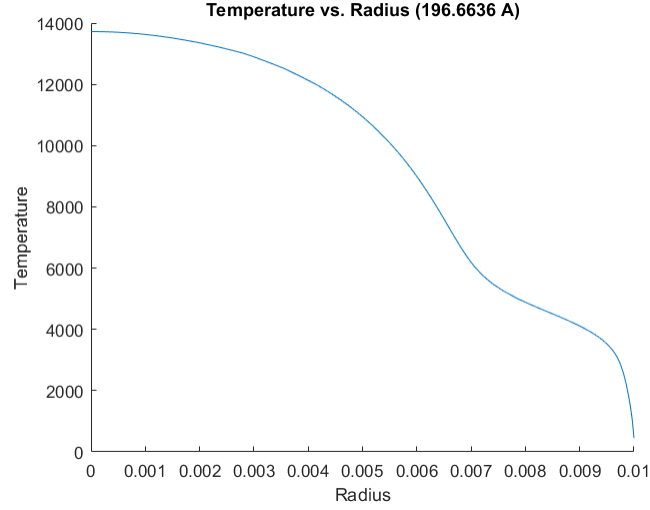
Next, the ramp function (piecewise linear) fit is performed on the electrical conductivity;



and using the fit parameters, the Elenbaas-Heller equation is solved to yield the arc radius as a function of current;



From the arc radius as a function of current, all other quantities of interest follow. For the current discussion, the most important of these are the radial temperature profiles and resulting radial composition maps.



# Appendix C

## Plasma Arc Simulation Code

---

```
filename = 'thesiscoalnew'; %The file which contains the MHD arc data
filename = strcat(filename, '.txt');
fid = fopen(filename);
FC = textscan(fid, '%s%s%s%s%s%s%s%s%s%s%s%s%s%s%s%s'); %as many
    strings as things
NTemps1 = size(FC{1}); %The number of temperatures examined, i.e. the
    number of things in each column
NTemps = NTemps1(1)-2;
fclose(fid);
N1 = size(FC);
N = N1(2); %The number of quantities of interest (maxes at 20?) from CEA

%Physical constants go here (all SI units)
Na = 6.022*10^23; %Avogadro's number
e0 = 8.85E-12; %Permittivity of space
kb = 1.38E-23; %Boltzmann's constant
qe = 1.60E-19; %Electron charge
me = 9.11E-31; %Electron mass
Qkerosone = 4.00E-19; %m^2

%Kerosene product cross sections
KC02 = 1.5E-19;
KC0 = 8.0E-20;
KH20 = 7.5E-19;
KO2 = 3.0E-20;
KO = 2E-19;
```

```

KK = 4E-18;
KKp = 0;

%Misc elements
KAr = 3.50E-21;
KH = 2.57E-19;
KH2 = 1.236E-19;

for i=1:N %This block generates the arrays of quantities that are present
    in all mixtures.
    if strcmp(FC{i}(1),'p')
        FC{i}(1) = [];
        FC{i}(NTemps+1)=[];
        pressures = str2num(char(FC{i}));
    end
    if strcmp(FC{i}(1),'t')
        FC{i}(1) = [];
        FC{i}(NTemps+1)=[];
        temps = str2num(char(FC{i}));
    end
    if strcmp(FC{i}(1),'rho')
        FC{i}(1) = [];
        FC{i}(NTemps+1)=[];
        rhos = str2num(char(FC{i}));
    end
    if strcmp(FC{i}(1),'cond')
        FC{i}(1) = [];
        FC{i}(NTemps+1)=[];
        thermcond = str2num(char(FC{i}));
    end
    if strcmp(FC{i}(1),'vis')
        FC{i}(1) = [];
        FC{i}(NTemps+1)=[];
        viscs = str2num(char(FC{i}));
    end
    if strcmp(FC{i}(1),'m')
        FC{i}(1) = [];
        FC{i}(NTemps+1)=[];
        MolarMass = str2num(char(FC{i})); %#ok<*ST2NM>
    end
    if strcmp(FC{i}(1),'e-')

```

```

FC{i}(1) = [];
FC{i}(NTemps+1)=[];
electrons = str2num(char(FC{i}));
end
end

thermcond=thermcond./10; %Unit conversion...

numSpec = 7; % MHD sample arc has 7 species
rawSpec = 'OH O2 O CO CO2 H2O K'; %These are the 7 species

species = textscan(rawSpec,'%s');
species = species{1,1};

totalSpec = zeros(NTemps,numSpec);

for i=1:numSpec %This block generates the arrays for the species
str = char(species(i));
for j=1:N
if strcmp(char(FC{j}(1)),str)
FC{j}(1) = [];
FC{j}(NTemps+1) = [];
foo = str2num(char(FC{j}));
totalSpec(:,i)=foo;
assignin('base', str , foo)
end
end
end

sumElem = zeros(NTemps,1);
for i=1:NTemps
sumElem(i)=sum(totalSpec(i,:));
end

sumAll = zeros(NTemps,1);
for i=1:NTemps
sumAll(i)=sum(totalSpec(i,:))+electrons(i);
end

```

```

Ntot = zeros(NTemps,1); %Calculate the total density
for i=1:NTemps
Ntot(i)=rhos(i)/MolarMass(i)*Na*1000;
end

Ne = zeros(NTemps,1); %Get the electron density
for i=1:NTemps
Ne(i)=Ntot(i)*electrons(i);
end

Nother = zeros(NTemps,1); %get the other density
for i=1:NTemps
Nother(i)=sumElem(i)*Ntot(i);
end

CoulombLog = zeros(NTemps,1); %Get the values for the Coulomb logarithm
for i=1:NTemps
    CoulombLog(i)=(12*pi/sqrt(Ne(i)))*(e0*kb*temps(i)/qe^2)^1.5;
end

IonCol = zeros(NTemps,1); %Get the ion collision term
for i=1:NTemps
IonCol(i)=3.9*Ne(i)*(qe^2/(8*pi*e0*kb*temps(i)))^2*log10(CoulombLog(i));
end

NeutralFactor = zeros(NTemps,numSpec); %Get the neutral collision term
for i=1:numSpec
for j=1:NTemps
if strcmp(species(i),'Ar')
NeutralFactor(j,i)=Ntot(j)*Ar(j)*KAr;
end
if strcmp(species(i),'CO')
NeutralFactor(j,i)=Ntot(j)*CO(j)*KCO;
end
if strcmp(species(i),'CO2')
NeutralFactor(j,i)=Ntot(j)*CO2(j)*KCO2;
end
if strcmp(species(i),'H2O')
NeutralFactor(j,i)=Ntot(j)*H2O(j)*KH2O;
end
if strcmp(species(i),'K')

```

```

NeutralFactor(j,i)=Ntot(j)*K(j)*KK;
end
if strcmp(species(i),'Kp')
NeutralFactor(j,i)=Ntot(j)*K(j)*KKp;
end
if strcmp(species(i),'O2')
NeutralFactor(j,i)=Ntot(j)*O2(j)*KO2;
end
if strcmp(species(i),'O')
NeutralFactor(j,i)=Ntot(j)*O(j)*KO;
end
if strcmp(species(i),'H')
NeutralFactor(j,i)=Ntot(j)*H(j)*KH;
end
if strcmp(species(i),'H2')
NeutralFactor(j,i)=Ntot(j)*H2(j)*KH2;
end
end
end

neutrals = zeros(NTemps,1);
for i=1:NTemps
neutrals(i)=sum(NeutralFactor(i,:));
end

condsub = zeros(NTemps,1); %Calculate the conductivity
for i=1:NTemps
condsub(i) =
    (Ne(i)*qe^2/me)/sqrt(8*kb*temps(i)/(pi*me))*1/(IonCol(i)+neutrals(i));
    %temperature
if isnan(condsub(i))
condsub(i)=0;
end
end

subplot(1,2,1)
hold on
plot(temps,condsub,'b','LineWidth',2);
%set(gca,'yscale','log')
ylabel('Electrical Conductivity (S/m)')
xlabel('Temperature')

```

```

title('Electrical Conductivity (\sigma)')
subplot(1,2,2)
hold on
plot(temps,thermcond,'r','LineWidth',2);
ylabel('Thermal Conductivity')
xlabel('Temperature')
title('Thermal Conductivity (\kappa)')

S = zeros(NTemps,1);

for i=2:NTemps %Generate the array of heat flux
S(i)=S(i-1)+(1/2)*(temps(i)-temps(i-1))*(thermcond(i-1)+thermcond(i));
    %Implicit, reference temp is 0 K
end

figure
plot(S,condsub,'-*')
ylabel('Electrical Conductivity')
xlabel('Heat Flux')
title('Electrical Conductivity vs. Heat Flux (to aid with fitting)')

% prompt4 = ['\n Please input a value for the heat flux near the linear
    region of the conductivity plot\n'...
%     'Note: the linear part must have a positive x-intercept. '];
% SLinear = input(prompt4);
SLinear = 1.6e4; %This works for the sample MHD arc; different values for
    different compositions
distanceS = zeros(NTemps,1);
for i=1:NTemps
distanceS(i)=S(i)-SLinear;
end
minDS=min(abs(distanceS)); %find the value of heat flux closest to the
    input value
for i=1:NTemps
if S(i)==minDS+SLinear || S(i)==SLinear-minDS
indexer = i;
break
end
end
end

```



```

condfit = zeros(1,5); %Perform the linear fit on the relevant part of the
    heat flux plot
Sfit = zeros(1,5);
for i=indexer:indexer+4
condfit(i-indexer+1)=condsub(i);
Sfit(i-indexer+1)=S(i);
end

Bfit = polyfit(Sfit,condfit,1);
S1=-Bfit(2)/Bfit(1); %Gives the value S1 defined by Gueye
B=Bfit(1); %Gives the value B defined by Gueye

S2fit = zeros(1,5); %Perform a fit to find the value S2 defined by Gueye
    (generally it's zero)
Temps2fit = zeros(1,5);
for i=1:5
S2fit(i) = S(i);
Temps2fit(i) = temps(i);
end
findS2 = polyfit(Temps2fit,S2fit,1);
S2 = findS2(1)*300+findS2(2);
if S2>0
return
else
S2=0;
end

TestCond = condsub; %How well does that linear fit actually work? We can
    eyeball.
for i = 1:N Temps
if S(i) < S1
TestCond(i) = 0;
else
TestCond(i) = B*(S(i)-S1);
end
end
figure
plot(S,condsub,'LineWidth',2);
%axis([0 2E5 0 4000])
ylabel('Electrical Conductivity (\sigma)')
xlabel('S (=\int \kappa dT)')

```

```

title('Electrical Conductivity vs. Heat Flux')
hold on
plot(S,TestCond,'LineWidth',2);
legend('Calculated','Piecewise-linear fit');

Imin = 3; %Discretize currents
Imax = 600;
numCurr = 20;

LNdI = (log(Imax)-log(Imin))/(numCurr-1);

I = zeros(numCurr,1); %"Actual" values
E = zeros(numCurr,1);
r0 = zeros(numCurr,1);

IStar = zeros(numCurr,1); %Non-dimensionalized quantities
Estar = zeros(numCurr,1);
rho = zeros(numCurr,1);

beta = 2.40483; %BesselJZero[0,1]
R = 0.01; %channel radius, meters

Smid = zeros(numCurr,1);
Tmid = zeros(numCurr,1);

SUnique = unique(S);
TUnique = unique(temps);

for i=1:numCurr

tempI = (i-1)*LNdI+log(Imin); %do the part where you calculate the other
    quantities
I(i) = exp(tempI);
IStar(i) = I(i)/((S1-S2)*sqrt(B)*R);

Ftemp = IStar*beta/(2*pi);

rho(i)=Ftemp(i)*lambertw(1/Ftemp(i)); %Rather than iterative guessing,
    use the Lambert W function

```

```

Estar(i)= beta/rho(i);
E(i)=Estar(i)/(sqrt(B)*R);

r0(i)=rho(i)*R;

Smid(i)=(S1-S2)/(log(1/rho(i))*beta*besselj(1,beta))+S1;
Tmid(i)=interp1(SUnique,TUnique,Smid(i));
end

figure
hold on;
plot(I,E,'-o');
ylabel('Electric Field (V/m)')
xlabel('Current (A)')
title('Electric field vs. Current')
figure
plot(I,Tmid,'-o');
ylabel('Axis Temperature (K)')
xlabel('Current (A)')
title('Axis Temperature vs. Current')
figure
plot(I,r0,'-o');
ylabel('Radius (r_0)')
xlabel('Current (A)')
title('Arc radius vs. Current')

%-----Off-axis stuff-----%

% currInterest = [1 5 10 15 20]; %Use this block if you want to see plots
%   at a variety of different currents
% figure
%
% for i=1:5
%   r0_Off=r0(currInterest(i));
%   rho_Off=rho(currInterest(i));
%   EStar_Off=Estar(currInterest(i));
%
%   Sin=@(r)
%       S1+(S1-S2)/(beta*besselj(1,beta)*log(1/rho_Off))*besselj(0,rho_Off*EStar_Off*r/r0_Off);

```

```

%      Sout=@(r)
%      S1-(S1-S2)/log(1/rho_Off)*log((1-(1-rho_Off)*(R-r)/(R-r0_Off))/rho_Off);
%
%      % figure
%      % fplot(@(r) Sin(r),[0 r0_Off],'b');
%      % hold on
%      % fplot(@(r) Sout(r),[r0_Off R],'b');
%      % ylabel('Heat Flux')
%      % xlabel('Radius')
%      % title('Heat Flux vs. Radius (at a given current)')
%
%      sampleRs = 500;
%      testR = linspace(0,R,sampleRs);
%      TOff = zeros(1,sampleRs);
%      crud = zeros(1,sampleRs);
%      for j=1:sampleRs
%          if testR(j)<r0_Off
%              TOff(j)=interp1(SUnique,TUnique,Sin(testR(j)));
%          else
%              TOff(j)=interp1(SUnique,TUnique,Sout(testR(j)));
%          end
%      end
%      hold on
%      plot(testR,TOff,'LineWidth',2);
%  end
%      ylabel('Temperature')
%      xlabel('Radius')
%      title('Temperature vs. Radius')
%      legend('3.0 A','9.15 A','36.9 A','148.8 A','600 A');

currInterest = 16; %Use this lock to see the values only at a
    representative current

r0_Off=r0(currInterest);
rho_Off=rho(currInterest);
EStar_Off=Estar(currInterest);

Sin=@(r)
    S1+(S1-S2)/(beta*besselj(1,beta)*log(1/rho_Off))*besselj(0,rho_Off*EStar_Off*r/r0_Off);
Sout=@(r)
    S1-(S1-S2)/log(1/rho_Off)*log((1-(1-rho_Off)*(R-r)/(R-r0_Off))/rho_Off);

```

```

%     Sintest=@(r)
%     S1-S1/(beta*besselj(1,beta)*log(rho_Off))*besselj(0,beta*r/(rho_Off*R));
%     Souttest=@(r) S1+S1/log(rho_Off)*log(r/(rho_Off*R));

figure
fplot(@(r) Sin(r),[0 r0_Off],'b');
hold on
fplot(@(r) Sout(r),[r0_Off R],'b');
ylabel('Heat Flux')
xlabel('Radius')
title('Heat Flux vs. Radius (at a given current)')

sampleRs = 100;
testR = linspace(0,R,sampleRs);
TOff = zeros(1,sampleRs);
crud = zeros(1,sampleRs);
for j=1:sampleRs
if testR(j)<r0_Off
TOff(j)=interp1(SUnique,TUnique,Sin(testR(j)));
else
TOff(j)=interp1(SUnique,TUnique,Sout(testR(j)));
end
end
figure
hold on
plot(testR,TOff);
ylabel('Temperature')
xlabel('Radius')
title(['Temperature vs. Radius (' num2str(I(currInterest)) ' A)'])

uniques = cell(1,numSpec);
eU = electrons;

for i=1:numSpec
tU = temps;
food = totalSpec(:,i);
for j=2:N Temps
if totalSpec(j,i)==totalSpec(j-1,i)
food(j)=food(j)+(1E-24)*rand;
end

```

```

if electrons(j)==electrons(j-1)
eU(j)=eU(j)+(1E-24)*rand;
end
end
uniques{i} = [food tU];
end

compMap = zeros(sampleRs,numSpec);
for i=1:numSpec
for j=1:sampleRs
toInterp = uniques{1,i};
compMap(j,i)=interp1(toInterp(:,2),toInterp(:,1),TOff(j));
end
end

electronMap=zeros(sampleRs,1);
for j=1:sampleRs
electronMap(j)=interp1(tU,eU,TOff(j));
end

legend_names = cell(1,numSpec); %Plots the composition map
figure
hold on;
for i=1:numSpec
plot(testR,compMap(:,i),'LineWidth',2);
legend_names{i} = species{i};
end
plot(testR,electronMap,'r','LineWidth',2);
set(gca, 'YScale', 'log')
axis([0 R 1E-11 1])
legend(species,'e^-+H^+')
ylabel('Concentration')
xlabel('Radius')
title(['Composition Map (' num2str(I(currInterest)) ' A)'])

potassiumMap = compMap(:,7); %For use in the index of refraction code

```

---

# Appendix D

## Index of Refraction Code

---

```
q = 1.6e-19; %electron charge
me = 9.11e-31; %electron mass
epsilon = 8.854e-12; %permittivity of free space
freq1 = 7.41815e14; %resonant frequency 1
freq2 = 7.41252e14; %resonant frequency 2
f1 = 5.69e-03; %oscillator strength of first resonance
f2 = 2.63e-03; %oscillator strength of second resonance
g1 = 1.16e+06; %damping of first resonance
g2 = 1.07e+06; %damping of second resonance
kb = 1.380e-23; %Boltzmann's constant
NTemps = 10;
m = 23*1.66e-27; %mass of nucleus
c = 3e8; %speed of light
N=5000; %Number of frequencies to test over

freqs=zeros(1,N); %Generate array of frequencies...
freqmin=freq2-0.0005e14;
freqmax=freq2+0.0005e14;
stepsize=(freqmax-freqmin)/N;

potassiumMap=compMap(:,7); %results taken from arc code
tempMap=TOff;
radius=testR;

for i=1:N
```

```

freqs(i)=freqmin+i*stepsize;
end
wls = zeros(1,N);
for i=1:N
wls(i)=c/freqs(i)*10^9;
end

wlsmin = min(wls); %... and wavelengths
wlsmax = max(wls);

temps = linspace(300,14000,NTemps);

%This generates the absorption coefficient (unbroadened)
a1 = @(x) f1*q^2*g1.*(x.^2)./(me*epsilon.*((x.^2-freq1^2).^2+g1^2*x.^2));
a2 = @(x) f2*q^2*g2.*(x.^2)./(me*epsilon.*((x.^2-freq2^2).^2+g2^2*x.^2));
at = @(x) a1(x)+a2(x);

a=zeros(1,N);

for i=1:N
a(i)=at(freqs(i));
end

%This generates the reactivity (unbroadened)
pn1 = @(x)
    f1*q^2*(freq1^2-x.^2)./(2*me*epsilon.*((x.^2-freq1^2).^2+g1^2*x.^2));
pn2 = @(x)
    f2*q^2*(freq2^2-x.^2)./(2*me*epsilon.*((x.^2-freq2^2).^2+g2^2*x.^2));
pn = @(x) pn1(x)+pn2(x);

n=zeros(1,N);
for i=1:N
n(i)=pn(freqs(i));
end

%Get the widths of the broadening profiles
delF1 = zeros(1,100); %Size should be as many radius sampling points as
    there are
delF2 = zeros(1,100); %Default is 100, from arc code
for i=1:100

```



```

delF1(i) = freq1/c*sqrt(2*kb*tempMap(i)/m);
delF2(i) = freq2/c*sqrt(2*kb*tempMap(i)/m);
end

maxF = max(potassiumMap); %get the density of potassium over radius
normalK=potassiumMap/maxF; %from the arc code
refDens = 10^23;
KDens = normalK*10^23;

%construct the broadening profiles
broadening=zeros(100,N);
prexp = zeros(100,N);
for i=1:N
for j=1:100
prexp(j,i)=-(freqs(i)-freq2).^2./delF2(j)^2;
end
end
for i=1:N
for j=1:100
broadening(j,i)=(1/sqrt(pi))*(1/delF2(j))*exp(prexp(j,i));
end
end

%Construct index of refraction and absorption coefficient
testa = zeros(100,100,N);
for j=1:100
for k=1:100
testa(k,j,:)=KDens(k)/N^2.*conv(a,broadening(j,:), 'same');
end
end

testnr = zeros(100,100,N);
for j=1:100
for k=1:100
testnr(k,j,:)=KDens(k)/N.*conv(n,broadening(j,:), 'same');
end
end

%consolidate to get just the radial map we want
amap = zeros(100,N);

```

```
nrmap = zeros(100,N);  
for i=1:100  
    for j=1:N  
        amap(i,j)=testa(i,i,j);  
        nrmap(i,j)=testnr(i,i,j);  
    end  
end
```

---

# Appendix E

## Ideal Wavelength Finder

---

```
y=0.005000000; %The value for y
N=10000; %the number of frequencies (from the index of refraction code)
% %----- find values of r0-----%
minrs = zeros(1,N);
diffs = zeros(N,numR);
n = zeros(N,numR);
for i=1:N
for j=1:numR
n(i,j)=1+nrmap(j,i);
end
end
for i=1:N
for j=1:numR
diffs(i,j)=radius(j)*n(i,j)-y;
end
end
mindexers=zeros(1,N);
findmin = abs(diffs);
for i=1:N
[value,index]=min(findmin(i,:)); %calculating values for r0
mindexers(i)=index;
end
for i=1:N
minrs(i)=radius(mindexers(i));
end
%-----%
```

```

integrand = zeros(N,numR);

for i=1:N
for j=1:numR %the integrand for the deflection integral
if radius(j)^2*n(i,j)^2>y^2
integrand(i,j)=(2*y/(radius(j)*sqrt(radius(j)^2*n(i,j)^2-y^2)));
end
end
end

rstep = radius(2)-radius(1); %integrate
deflections = zeros(numR,N);
for i=1:N
deflections(:,i)=cumtrapz(integrand(i,:));
end

deffles = zeros(1,N);
for i=1:N
deffles(i) = deflections(numR,i);
end

sympoint = N/2-1; %make a value corresponding to the absolute value of
    deflection
symmeter = zeros(1,N);
for i=1:N
symmeter(i) = deffles(sympoint)+abs(deffles(i)-deffles(sympoint));
end

pathlength=0.02; %estimate the absorption factor
absfac = zeros(1,N);
for i=1:N
absfac(i)=0.02*0.5*max(amac(:,i));
end

zetaweight = 0.1;

utilityF = zeros(1,N); %generate the utility function
for i=1:N
if absfac(i)<4.6
utilityF(i)=symmeter(i)-zetaweight*absfac(i);

```

```

end
if absfac(i)>4.6
utilityF(i)=0.99999*utilityF(1); %actually sending to zero wrecks the
    plot area for visualization purposes, use this instead
end
end
% for i=1:N %another possible utility function
%     if absfac(i)<4.6
%         utilityF(i)=deffles(i)/(1+zetaweight*absfac(i));
%     end
%     if absfac(i)>4.6
%         utilityF(i)=0.99999*utilityF(1);
%     end
% end

plot(wls,utilityF)
axis([wlsmin wlsmax 6.0528E4 6.05295E4]);

[maxU, indU]=max(utilityF);

wlideal1 = wls(indU) %get the two ideal wavelengths
wlideal2 = wls(sympoint)+wls(sympoint)-wls(indU)

```

---